



Universitá degli Studi di Padova

Dipartimento di Scienze Fisiche

Corso di Laurea Magistrale in Scienza dei Materiali

**Quantum Optics Experiments with Single
Nitrogen-Vacancy Centers in Nanodiamonds**

Laureando

Nikola Sadzak

Relatore

Prof. Alberto Carnera

Co-relatore

Prof. Oliver Benson

Abstract

The second half of the XX century was distinguished by the development of various scientific and technological fields related to quantum mechanics. One of the most ambitious is Quantum Information Processing, placed between theoretical and applied physics, informatics and engineering. Its aim is to take advantage of elementary particles quantum properties to represent information and process it according to logical schemes. In 1995, it has been proven that a quantum computer could be realized by using only indistinguishable single photons and linear optics elements. Such model requires specific emitters capable of generating indistinguishable photons on demand. Color centers in diamond were one of the first candidates in this framework. In particular, the negatively charged nitrogen-vacancy defect (NV) center in bulk diamond has been considered attractive as it provides a narrow zero phonon line (ZPL) at the optical transition at 637 nm and it's stable even at room temperature. However, for integrated solid state devices, representing logical circuits in the LOQC framework, nano-diamonds with single NV centers are preferable as they can be manipulated and integrated in different photonic structures. Here, a major problem is the inhomogeneous broadening of the ZPL due to environmental fluctuations. Performing photon correlation interferometry measurements, we determine the spectral diffusion time-scale as function of different excitation conditions (temperature, power, and color) in order to gain further knowledge about the underlying processes, as also estimate the suitability of such emitter for QIP applications.

Contents

List of acronyms	5
1 Introduction	7
1.1 Historical Background	7
1.2 Quantum Computation	8
1.3 Physical Implementation	12
1.4 Linear Optics Quantum Computer	13
1.5 Motivation and Outline	16
2 Theory of Photon Statistics	17
2.1 Introduction to a Quantum Model of Light	17
2.2 The Photon Detection Process	23
3 Solid State Single Photon Sources	29
3.1 Colour Centers in Wide Bandgap Materials	29
3.2 Diamond Structure and General Properties	31
3.3 Diamond Classification	31
3.4 The Nitrogen-Vacancy Center Structure	32
3.5 Energy Levels of the NV Center	38
3.6 Optical Transitions: Selection Rules and Spectra	40
3.7 NV Centers in Nanodiamonds	44
4 Line broadening in Photon Emitters	47
4.1 Two Level Systems and Single Photon Wavepackets	47
4.2 Decoherence Processes in Single Photon Emission	51
4.3 The Homogeneous Broadening Limit	54
4.4 The Inhomogeneous Broadening Limit	55

5 Photon Correlation Interferometry	57
5.1 Mach-Zehnder Interferometer	59
5.2 Photon Correlation Interferometry Setup	61
5.3 Spectral Diffusion Characteristic Time	62
6 The Experimental Setup	67
6.1 Solid Immersion Lenses	67
6.2 Sample Description and Preparation	70
6.3 General Setup Scheme	72
6.4 Cryostat	73
6.5 Excitation Line	74
6.6 Optical Section	75
6.7 Camera	76
6.8 Mach-Zehnder Interferometer	76
6.9 APD Detectors and Counting Module	76
6.10 Spectrograph	77
6.11 Device Interface and Automatization	77
7 Measuring Spectral Diffusion	79
7.1 Sample Preparation and Check	79
7.2 Cryostat Setup	82
7.3 Single Spectral Diffusion Measurement Procedure	82
7.4 Power Dependency Measurements	87
7.5 Temperature Dependency	89
7.6 Color Dependency Measurement	90
7.7 Result Summary	91
8 Outlook and Conclusions	93
Bibliography	95

List of acronyms

APD	avalanche photodiode
a.u.	arbitrary units
BP	bandpass
CCD	charge-coupled device
cts	counts
CVD	chemical vapour deposition
CW	continuous wave
EM	electromagnetic
EPR	Einstein-Podolsky-Rosen
i.e.	id est (that is)
IRREP	irreducible representation
ISC	intersystem crossing
HBT	Hanbury-Brown-Twiss
HOM	Hong-Ou-Mandel
LED	light emitting diode
LP	long pass
NA	numerical aperture
NDIA	nanodiamonds
PSB	phonon side bands

Chapter 1

Introduction

1.1 Historical Background

The XX century saw the appearance of quantum mechanics as a new paradigm for the understanding of the physical world, in particular on the atomic scale. Experimental evidences being in contradiction to classical mechanics and electrodynamics, brought scientists to a new model of the physical reality. In this revolutionary model concepts and principles as wave-particle duality, discretization of certain physical properties and uncertainty relations between specific observables play a fundamental role. The new intrinsically probabilistic approach to describe the behaviour of particles needed the development of a particular mathematical formalism: quantum mechanics. As the new paradigm gained popularity, it was merged with Einstein's relativity into the quantum field theories. Later on, phenomena as entanglement and the non locality of quantum mechanics were object of a wide debate among the physics community [1,2]. This debate could partially be solved in favour of the copenhagen interpretation of quantum mechanics by striking experimental evidence in the '80s [3]. In parallel, the new theory proved to have an enormous success in explaining and modelizing the microscopic world. It described the behaviour of atomic and sub-atomic particles more precise than any theory before, and was profitably applied in the fields of condensed matter physics, particle physics, solid-state physics, chemistry, materials science, engineering and indirectly in many others. The beginning of the '80s saw the appearance of a new sector: the quantum information

processing. Placed between physics, informatics, engineering and materials science, it deals (in the most general terms) with the processing of information by exploiting the theoretical framework of quantum mechanics and using physical systems on which these laws can be applied. The topic itself can be distinguished into the major fields of quantum communication and computation. For the purpose of this thesis, an short introduction to the latter will be given.

1.2 Quantum Computation

Quantum information processing means performing logical operations on some data using the particular features of quantum mechanics to represent and transform them according to a logical scheme [4]. A universal device that implements these functionalities is called quantum computer. The fundamental unit of such a model is the qubit, a vector-state ψ defined on a 2-dimensional Hilbert space, to which a general information can be associated:

$$|\psi\rangle = \alpha_0 |0\rangle + \alpha_1 |1\rangle = \begin{pmatrix} \alpha_0 \\ \alpha_1 \end{pmatrix} \quad (1.1)$$

Where α_0 and α_1 are two complex numbers satisfying the normalization condition:

$$|\alpha_0|^2 + |\alpha_1|^2 = 1 \quad (1.2)$$

While a classical bit can carry on only the logical values of 0 or 1 , the quantum bit represented by the complex vector $|\psi\rangle$ can be every superposition (linear combination) of the basis vectors 0 and 1 that follows the condition (1.2). The Bloch sphere is an intuitive representation of this system:

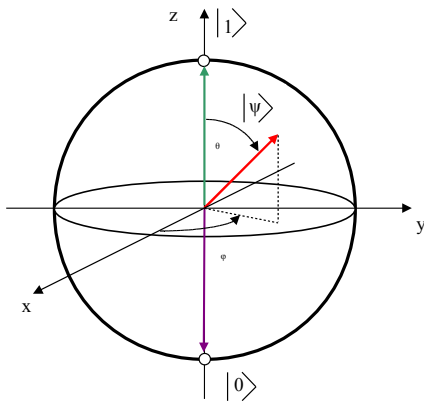


Figure 1.1: Image of a Bloch Sphere with a generic ψ vector represented as a linear combination of the two basis states

Since a one-qubit state is defined on a 2-dimensional Hilbert space, an N qubit state is defined on an $2N$ -dimensional space. Thus it is a superposition of $2N$ orthogonal basis vectors with normalized coefficients:

$$|\psi\rangle = \alpha_{00} |00\rangle + \alpha_{01} |01\rangle + \alpha_{10} |10\rangle + \alpha_{11} |11\rangle \quad (1.3)$$

$$|\alpha_{00}|^2 + |\alpha_{01}|^2 + |\alpha_{10}|^2 + |\alpha_{11}|^2 = 1 \quad (1.4)$$

It is important to notice that a state obtained i.e. from the product of two qubit states is only a particular case of the former expression (1.3):

$$\begin{aligned} |\psi\rangle &= |\psi_\alpha\rangle \otimes |\psi_\beta\rangle = \\ &= (\alpha_0 |0\rangle + \alpha_1 |1\rangle) \otimes (\beta_0 |0\rangle + \beta_1 |1\rangle) = \\ &= \alpha_0\beta_0 |00\rangle + \alpha_0\beta_1 |01\rangle + \alpha_1\beta_0 |10\rangle + \alpha_1\beta_1 |11\rangle \end{aligned} \quad (1.5)$$

So it can be seen that (1.3) corresponds to (1.5) only if the additional condition:

$$\alpha_{00}\alpha_{11} = \alpha_{01}\alpha_{10} \quad (1.6)$$

is satisfied, as in (1.3), the α_{xy} set of coefficients must obey only the overall normalization condition, while in (1.5) they are inherently related via (1.6). This means, that a N -qubit state cannot be generally expressed as a product of a set made by N single-qubit states, since it might contain superpositions for which an individual qubit is not characterized by a pure

state but is rather entangled (correlated) with other qubits. This purely non-classical feature determines the power of computation on multi-qubit states and outlines the qubit manipulation process.

In a quantum circuit used for information processing, logical operations are performed on the quantum bits by different sequences of quantum gates; these objects execute reversible, norm-preserving linear transformations on the qubits, which can be seen as rotations of the ψ vector on the Bloch sphere. They are mathematically represented as unitary operators acting on Hilbert space. It can be proven [5] that these operators, if acting on N -qubits, can be decomposed in sequences of single and two-qubit operators: this property will have a high impact on the technological realization of such a computational devices. A single-qubit operator is i.e. the Hadamard gate, which maps the two basis states $|0\rangle$ and $|1\rangle$ in superpositions according to the matrix:

$$H = \frac{1}{\sqrt{2}} \begin{pmatrix} 1 & 1 \\ 1 & -1 \end{pmatrix} \quad (1.7)$$

This means that the $|0\rangle$ and $|1\rangle$ basis vectors are mapped into:

$$|0\rangle \longrightarrow \frac{|0\rangle + |1\rangle}{\sqrt{2}} \quad (1.8a)$$

$$|1\rangle \longrightarrow \frac{|0\rangle - |1\rangle}{\sqrt{2}} \quad (1.8b)$$

On the other side, an example of 2-qubit gate is the *cNOT*. The two-qubit character stems from the fact that a first qubit, the control value, gives the condition for the operation on the second qubit, according to the truth table:

a	b	a'	b'
0	0	0	0
0	1	0	1
1	0	1	1
1	1	1	0

Table 1.1: Truth table for the CNOT gate, being $|a\rangle |b\rangle$ the input qubits and $|a'\rangle |b'\rangle$ the output states

So, if the control bit is zero, the value of the data-bit remains unchanged, otherwise it is flipped. In general terms, every operation U_f can be represented as an action on a state defined with n input bases which brings to an outcome expressed with m output bases, as below:

$$U_f (|x\rangle_n |y\rangle_m) = |x\rangle_n |y \oplus f(x)\rangle_m \quad (1.9)$$

With \oplus indicating a bitwise exclusive *OR* operation. If the output registers y are initialized to a null value, the (1.9) becomes:

$$U_f (|x\rangle_n |0\rangle_m) = |x\rangle_n |f(x)\rangle_m \quad (1.10)$$

Now, by creating an input set of n 0-valued x states, and subsequently applying $H^{\otimes n}$ Hadamard gates, a state made by a combination of all the possible input states is obtained [6]:

$$H^{\otimes n} |0\rangle_n = \frac{1}{2^{n/2}} \sum_{0 \leq x \leq 2^n} |x\rangle_n \quad (1.11)$$

If any U_f transformation is afterwards applied, an interesting feature of quantum computing is observed:

$$U_f (H^{\otimes n} \otimes 1^m) (|0\rangle_n |0\rangle_m) = \frac{1}{2^{n/2}} \sum_{0 \leq x \leq 2^n} |x\rangle_n |f(x)\rangle_m \quad (1.12)$$

The physical meaning is that with a single computational passage, one can obtain simultaneously the 2^n values of the f function encoded in the final state [6]. This powerful result, called quantum-parallelism, is a major feature of a quantum computer, and it shows which kind of improvements can be reached. Unfortunately, this scheme has a main disadvantage: as we have seen, the output of the elaboration is indeed encoded in a state which consists of m entangled single-qubits. Thus, the associated information is not immediately available to the observer. Where a set of classical bits needs to be only *observed* in order to extract the data from it, in the quantum world a *measurement* must be performed on the qubits. This is specifically a projective measurement, and which will make the ψ state-vector collapse on one of its subspaces (ψ will assume therefore a particular value) with

a probability equal to the squared module of its coefficient. Once a single measurement is done, the ψ state will lose every information and memory relative to the other states of the superposition. Thus, only one outcome can be non-deterministically obtained from the qubit while the measure itself has a destructive character. However, this problem can be controlled by using specific algorithms[7], that add still some relevant complexity to the device. Nevertheless, it has been proven [8] that certain computational tasks (like searching algorithms, factorizations of numbers, simulations of quantum systems) are solved on a quantum computer with linear or polynomial scalability versus the number of input-variables involved, where a classical machine would require an exponential amount of resources (and thus time) to perform the same tasks. Another important issue that has to be considered is decoherence [9], i.e. the coupling of an initially isolated quantum system to the environment. This introduces losses of the relative phases between the base-states and translates into computational errors. In order to limit such behaviour, an accurate choice of the physical system that will implement the qubits and the logical gates must be done.

Five fundamental criterias, useful in the selection process of a physical system functional for the realization of a quantum computer, were enunciated in [10].

1.3 Physical Implementation

The implementation of a quantum computer is subject to some main requirements, according to the *DiVincenzo* model [10].

- There must be a physical entity that can represent a qubit. As an example, the polarization state of a single photon (Horizontal or Vertical), or a single electron spin state (up/down).
- Initialization of qubits with a certain value has to be permitted (I.E., a set of spin-down mutually isolated electrons).
- Decoherence times shall be higher than gate operation times: a specific quantum state must not interact with the environment as long as the elaboration is running otherwise the information are irreversibly lost.

- The implementation of a set of universal quantum gates (either single or two-qubit) has to be possible. In other words, there must be a way to manipulate qubits in a controlled way.
- It must be allowed to perform a projective measurement on one or more (entangled) qubits, in order to extract information from them.

Few solutions have been found in the past 20 years and developed in parallel. In this thesis a specific framework will be adopted, that is the *linear optics quantum computer* suggested by *Knill, Laflamme and Milburn* in 2001 [11].

1.4 Linear Optics Quantum Computer

Different photon modes can be used to represent qubits. This can be either through their polarization states or their spacial states. The simplest association in case of spatial encoding is:

$$\begin{aligned} |0\rangle &= |0\rangle_l |1\rangle_m \\ |1\rangle &= |1\rangle_l |0\rangle_m \end{aligned} \tag{1.13}$$

So a qubit in state $|0\rangle$ can be represented by *zero* photons in mode l and one in mode m ; viceversa the orthogonal state consists of one photon in l -mode and none in m -mode. Thus, the overall state is written as it follows:

$$\begin{aligned} |\psi\rangle &= \alpha_0 |0\rangle_l |1\rangle_m + \alpha_1 |1\rangle_l |0\rangle_m = \\ &= \alpha_0 |01\rangle_{lm} + \alpha_1 |10\rangle_{lm} \end{aligned} \tag{1.14}$$

The Hamiltonian describing a free photon in mode l is:

$$H = \hbar\omega a^{(l)\dagger} a^{(l)} \tag{1.15}$$

Where $a^{(l)\dagger}$ and $a^{(l)}$ are the creation and annihilation operators for a photon of ω frequency and l mode (more details are given in Chapter 2). Recently, it has been proven [11,12] that single and two qubit gates can be constructed by only using linear optical elements such as phase shifters and beamsplitters. These objects act on the creation operators of the photons, preserving

(except in case of losses due to non-ideal conditions) their overall number. In example, we might consider the unitary matrix representing a beam-splitter and the transformation it makes on a specific input state, which is exactly the operation performed by a Hadamard Gate:

$$U_{BS} = \frac{1}{\sqrt{2}} \begin{pmatrix} 1 & 1 \\ 1 & -1 \end{pmatrix} \quad (1.16)$$

If we start with $|1\rangle_l |0\rangle_m = \begin{pmatrix} 1 \\ 0 \end{pmatrix}$, what we obtain as output is:

$$U_{BS} \begin{pmatrix} 1 \\ 0 \end{pmatrix} = \frac{1}{\sqrt{2}} \begin{pmatrix} 1 & 1 \\ 1 & -1 \end{pmatrix} \begin{pmatrix} 1 \\ 0 \end{pmatrix} = \frac{1}{\sqrt{2}} \begin{pmatrix} 1 \\ 1 \end{pmatrix} \quad (1.17)$$

Where the final state is a combination of the two initial photon modes. A central issue in the KLM scheme is the fact that, in order to have two-qubit gates, one has to find a way to make different photons (qubits) interact among each other. One idea is to use non-linear medias that would recombine the creation operators according to the Hamiltonian:

$$H = -\chi a^{(l)\dagger} a^{(l)} a^{(m)\dagger} a^{(m)} \quad (1.18)$$

Where χ is the coupling constant. Under certain conditions this phenomena is called *Kerr-effect*. The drawback arises from the poor availability of materials showing a sufficiently strong coupling factor. Therefore an alternative solution was found in the Hong-Ou-Mandel effect [13]: this is a two photon interference effect that creates a maximally entangled state by simply sending two indistinguishable photons in a lossless 50:50 beamsplitter.

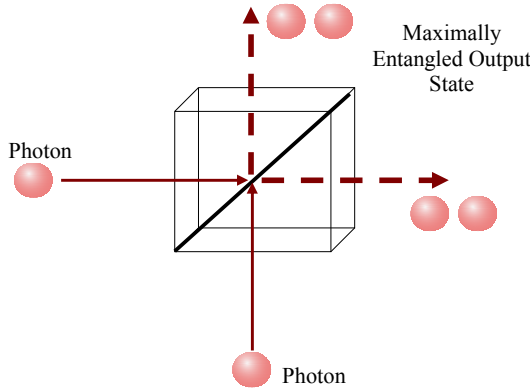


Figure 1.2: A scheme representing the Hong-Ou-Mandel effect with particle-behaving photons that exit the beamsplitter in bunches

Having two photons in separate spatial modes coming at the beamsplitter as in Fig. 1.2, and considering the unitary transformation that is applied to the creation operators by the latter, the so obtained final is:

$$\begin{aligned} |11\rangle_{lm} &= a^{(l)\dagger} a^{(m)\dagger} |00\rangle_{lm} \xrightarrow{U_{BS}} \frac{1}{2} (a^{(f)\dagger} + a^{(g)\dagger}) (a^{(f)\dagger} - a^{(g)\dagger}) |00\rangle_{fg} \\ &= \frac{1}{2} \left((a^{(f)\dagger})^2 - (a^{(g)\dagger})^2 \right) |00\rangle_{fg} = \frac{1}{\sqrt{2}} \left(|20\rangle_{fg} - |02\rangle_{fg} \right) \end{aligned} \quad (1.19)$$

The physical meaning of (1.19) is that the two elementary light particles exit the beamsplitter always in the same spatial mode, that can be either f or g ; they will exit in a *bunched* and entangled state. Such correlation allows the construction, with some practical expedients, of universal sets of quantum gates using, as mentioned, only linear optical elements. For the details, see[14,15]. After the logical operations have been carried on, the output of the computational task is stored in a single or multi-qubit physical state, so in a set of photons with different spatial modes. Therefore, a measurement has to be done. In the KLM model this implies that photons in certain modes must be revealed by means of single photon detectors. On the other side, qubit initialization relies on the availability of single photon sources. This sources shall be able to generate indistinguishable photons on demand, and shall be stable in time; the optical characterization of a solid state single photon source will be the main topic of this thesis.

1.5 Motivation and Outline

The purpose of this work is to evaluate the optical activity of Nitrogen-vacancy defect centers in nanodiamonds for the role of QIP-dedicated stable sources of single and indistinguishable photons, generated via photoexcitation. The NV center is a point defect in diamond lattice with a specific electronic and energetic configuration that gives a three-level system behaviour [16]. The Zero-Phonon-Line of the most relevant transition is located at 637 nm; a radiative decay from the excited state to the ground state implies the emission of one photon per cycle. The lifetime limited linewidth, in bulk diamond, has been determined in circa 13 Mhz (where the emission line has a frequency of 470 Thz) . Nevertheless, the experimental evidence shows that the same ZPL is inhomogeneously broadened to $0,5 \div 1,0$ nm, fact that could compromise any possibility to see a Hong-Ou-Mandel effect. Therefore, an interferometric method is here developed in order to measure the time-scale of the spectral diffusion process in the ZPL; from this result, an evaluation of the success probability for the HOM effect can be estimated. In Chapter 2, some fundamentals of photon statistics are given, on the purpose of having few theoretical models to use in the characterization of different photon emission regimes. Chapter 3 presents in detail the physical system chosen as single photon source, so the NV center in diamond and nanodiamond. Subsequently, in chapter 4 the photon indistinguishability criterias and the emission line features are discussed. In chapter 5 we present an interferometric method used to measure the inhomogeneous broadening timescale, while in chapter 6 the required experimental setup is shown. In chapter 7 the operative method adopted to collect data and the relative results are presented. Finally, in chapter 8 the experimental outcomes are discussed and some perspectives for nanodiamond-based nitrogen-vacancy centers in QIP applications are given, with the eventual further developments.

Chapter 2

Theory of Photon Statistics

2.1 Introduction to a Quantum Model of Light

The first complete theory of the electromagnetism was formulated by Maxwell in the second half of the *XIX* century, and can be summarized in the well known non-relativistic equations. In vacuum state, these are written as:

$$\nabla \cdot \mathbf{E} = 0 \quad (2.1a)$$

$$\nabla \cdot \mathbf{B} = 0 \quad (2.1b)$$

$$\nabla \times \mathbf{E} = -\frac{\partial \mathbf{B}}{\partial t}, \quad (2.1c)$$

$$\nabla \times \mathbf{B} = \frac{1}{c^2} \frac{\partial \mathbf{E}}{\partial t} \quad (2.1d)$$

where \mathbf{E} represents the electric field, \mathbf{B} the magnetic field and c the speed of light. Introducing the potential vector \mathbf{A} , and remembering that Φ is a scalar field, we have:

$$\mathbf{B} = \nabla \times \mathbf{A} \quad (2.2a)$$

$$\mathbf{E} = -\nabla \Phi - \frac{1}{c} \frac{\partial \mathbf{A}}{\partial t} \quad (2.2b)$$

and assuming the Coulomb gauge:

$$\nabla \cdot \mathbf{A} = 0 \quad (2.3)$$

it is possible to obtain a wave equation from the previous set:

$$\nabla^2 \mathbf{A} = \frac{1}{c^2} \frac{\partial^2 \mathbf{A}}{\partial t^2} \quad (2.4)$$

One of the solutions for the (2.4) are plane waves of the form:

$$\mathbf{A}(\mathbf{r}, t) = \sum_k \sqrt{\frac{\hbar}{2\epsilon_0\omega_k}} [A_k(t) \mathbf{u}_k(\mathbf{r}) + A_k^*(t) \mathbf{u}_k^*(\mathbf{r})] \quad (2.5)$$

Where ϵ_0 is the vacuum perittivity and the potential vector is expanded over his Fourier components with coefficients:

$$A_k(t) = a_k e^{-i\omega_k t} \quad (2.6)$$

and the spatial dependence is given by a set of orthonormal vectors $\mathbf{u}_k(\mathbf{r})$:

$$\mathbf{u}_k(\mathbf{r}) = \frac{1}{V} \xi e^{i\mathbf{k}\mathbf{r}} \quad (2.7)$$

In the last expression, V is a normalization condition that accounts for the volume of the field mode and ξ represents the polarization orientation. The electromagnetic field has an energy whose flux density is indicated by the Poynting vector:

$$\mathbf{S} = \frac{1}{\mu_0} \mathbf{E} \times \mathbf{B} \quad (2.8)$$

And the associated Hamiltonian is:

$$H = \frac{1}{2} \int d^3r \left[\left(\frac{\partial \mathbf{A}}{\partial t} \right)^2 \epsilon_0 + \frac{1}{\mu_0} (\nabla \times \mathbf{A})^2 \right] \quad (2.9)$$

with μ_0 being the vacuum magnetic permeability. By introducing a set of coniugated coordinates and momenta, calculated from the Fourier expansion coefficients:

$$q_k(t) = \sqrt{\frac{\hbar}{2\omega_k}} (A_k(t) + A_k^*(t)) = \sqrt{\frac{\hbar}{2\omega_k}} (a_k e^{-i\omega_k t} + a_k^* e^{i\omega_k t}) \quad (2.10a)$$

$$p_k(t) = -i\sqrt{\frac{\hbar\omega_k}{2}} (A_k(t) - A_k^*(t)) = -i\sqrt{\frac{\hbar\omega_k}{2}} (a_k e^{-i\omega_k t} - a_k^* e^{i\omega_k t}) \quad (2.10b)$$

One can rewrite the Hamiltonian for an electromagnetic field in a form that resembles the Hamiltonian of an harmonic oscillator:

$$\begin{aligned} H &= \frac{1}{2} \int d^3r \left[\left(\frac{\partial \mathbf{A}}{\partial t} \right)^2 \varepsilon_0 + \frac{1}{\mu_0} (\nabla \times \mathbf{A})^2 \right] = \\ &= \sum_k \left[\frac{p_k^2}{2} + \frac{\omega_k^2}{2} q_k^2 \right] \end{aligned} \quad (2.11)$$

The quantization can be obtained by substituting the classical q_k and p_k quantities with their quantum counterparts, in order to obtain the anticommutative relation:

$$[\hat{q}_k, \hat{p}_{k'}] = i\hbar\delta_{k,k'} \quad (2.12)$$

Therefore, we can introduce from (2.10)s the creation and annihilation anticommutative operators, obeying the relation $[\hat{a}_k, \hat{a}_{k'}^\dagger] = \delta_{k,k'}$:

$$\hat{a}_k = \frac{1}{\sqrt{2\omega_k}} (\omega_k \hat{q}_k + i\hat{p}_k) \quad (2.13a)$$

$$\hat{a}_k^\dagger = \frac{1}{\sqrt{2\omega_k}} (\omega_k \hat{q}_k - i\hat{p}_k) \quad (2.13b)$$

The field Hamiltonian is therefore written as:

$$\hat{H} = \int d^3k \left\{ \hat{a}_k \hat{a}_k^\dagger + \frac{1}{2} \right\} \hbar\omega_k \quad (2.14)$$

To simplify the model, we will leave aside the polarization notation and consider a single-frequency and single-mode field in an ideal cavity, with fixed boundary conditions. From the (2.14) and (2.13) expressions, it is possible to derive a general photon number operator:

$$\hat{N}(k) = \hat{a}_k^\dagger \hat{a}_k \quad \hat{N}(k) = \frac{1}{\hbar\omega_k} \hat{H}_k - \frac{1}{2} \quad (2.15)$$

which, as the Hamiltonian, is Hermitian, and can be used to set up an analogous eigenvalue equation:

$$\hat{N}|n\rangle = n|n\rangle \quad (2.16)$$

with $|n\rangle$ being the eigenvectors of \hat{N} with n eigenvalues. The annihilation and creation operators act on the $|n\rangle$ vectors by transforming them into new ones, that means, they raise or lower the number of quanta (photons) in a certain light mode and frequency with no limit to their number for a specific dynamical mode (they are bosonic operators). Assuming that:

$$\hat{a} |0\rangle = 0 \quad (2.17)$$

the eigenstates one can find for the previous problem are:

$$|n\rangle = \frac{1}{\sqrt{n!}} (\hat{a}^\dagger)^n |0\rangle \quad (2.18)$$

and are called *Fock* or *number* states. They have also the property of showing no variance of the photon number:

$$\langle \Delta n^2 \rangle = \langle n | \hat{N}^\dagger \hat{N} | n \rangle - \langle n | \hat{N} | n \rangle^2 = 0 \quad (2.19)$$

For a general electromagnetic field, the photon distribution in time can be obtained via a counting measurement. While the experimental details will be discussed below, we will note here that a counting measurement is in fact a square normed projection of a certain light state vector on a photon number basis:

$$P_\psi(n) = |\langle n | \psi \rangle|^2 \quad (2.20)$$

As mentioned above, the Fock state has zero variance. Thus, it describes an exact photon number, stationary in time. Another interesting case is represented by the coherent states. In fact, these are eigenstates of a photon annihilation operator, with complex eigenvalues α :

$$\hat{a} |\alpha\rangle = \alpha |\alpha\rangle \quad (2.21)$$

They are indeed states with the lowest possible uncertainty observable in their phase-space. Coherent states can be expressed as a linear superposition of Fock states, as it's shown below:

$$|\alpha\rangle = e^{-\frac{1}{2}|\alpha|^2} \sum_n \frac{\alpha^n}{\sqrt{n!}} |n\rangle \quad (2.22)$$

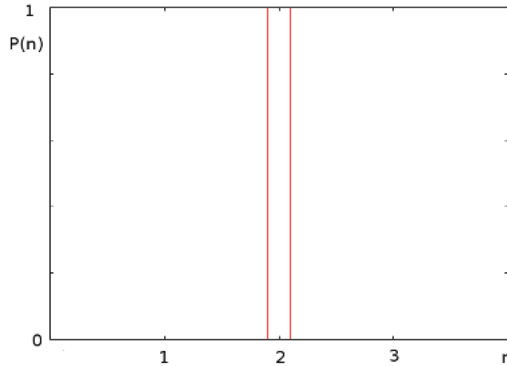


Figure 2.1: Graph of a Fock state probability distribution: the variance is zero, and the state is characterized by a definite number of photons

By calculating the square norm of the $|\alpha\rangle$ eigenvector projected on a specific number state, one can obtain the probability to have that number of photons in the field:

$$P_\alpha(n) = |\langle n | \alpha \rangle|^2 = \frac{e^{-|\alpha|^2} |\alpha|^{2n}}{n!} \quad (2.23)$$

It is possible to notice that $P_\alpha(n)$ follows a poissonian distribution and so is called the electromagnetic radiation that shows this feature. A source of coherent light will therefore emit an average number of photons given by:

$$\langle n \rangle = \langle \alpha | \hat{N} | \alpha \rangle = |\alpha|^2 \quad (2.24)$$

with variance:

$$\langle \Delta n^2 \rangle = \langle \alpha | \hat{N}^\dagger \hat{N} | \alpha \rangle - \langle \alpha | \hat{N} | \alpha \rangle^2 = |\alpha|^2 \quad (2.25)$$

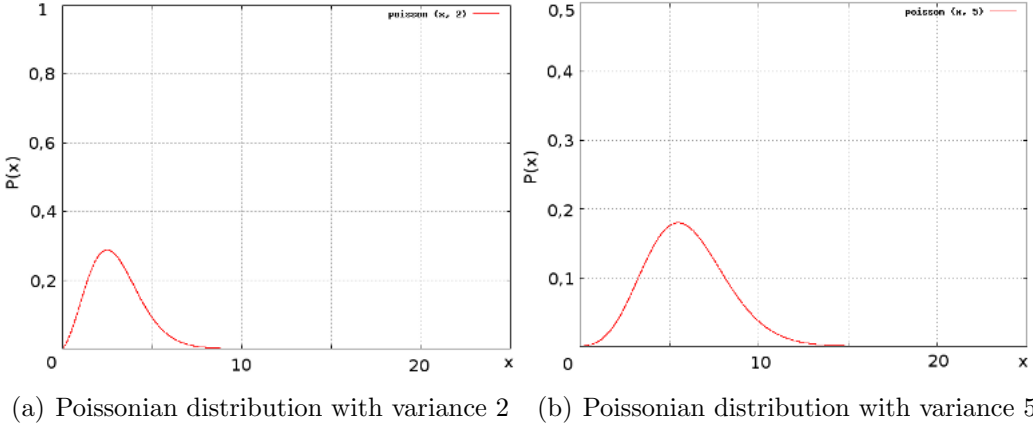


Figure 2.2: The graphs depict two poissonian distributions of given variance and expectation value, which are equal in such statistics

The further case of thermal (chaotic) light can be seen as a nonlinear superposition of Fock states with coefficients deduced from the Bose-Einstein distribution. This non-pure state is described by the density matrix:

$$\hat{\rho}_T = \sum_{n=0}^{n=\infty} e^{-\frac{\hbar\omega n}{k_b T}} \left[1 - e^{-\frac{\hbar\omega}{k_b T}} \right] |n\rangle \langle n| \quad (2.26)$$

Where the probability to have a certain photon number in the radiation is given by:

$$P_{\rho_T}(n) = e^{-\frac{\hbar\omega n}{k_b T}} \left[1 - e^{-\frac{\hbar\omega}{k_b T}} \right] \quad (2.27)$$

The average number of photons associated is:

$$\langle n \rangle = Tr \left[\hat{\rho}_T \hat{N} \right] = \left[e^{\frac{\hbar\omega}{k_b T}} - 1 \right]^{-1} \quad (2.28)$$

And the corresponding variance can be calculated as it follows:

$$\begin{aligned} \langle \Delta n^2 \rangle &= Tr \left[\hat{\rho}_T \hat{N}^\dagger \hat{N} \right] - \left(Tr \left[\hat{\rho}_T \hat{N} \right] \right)^2 = \\ &= \langle n \rangle^2 + \langle n \rangle = \\ &= \left[e^{\frac{\hbar\omega}{k_b T}} - 1 \right]^{-2} + \left[e^{\frac{\hbar\omega}{k_b T}} - 1 \right]^{-1} \end{aligned} \quad (2.29)$$

Many more states of light can be identified, although for the purpose of this work they don't need to be explicitly mentioned. A vast literature

is indeed available [17, 18, 19, 20]. However, a first characterization of an electromagnetic field statistics can be deduced in a very simple way from the Fano factor [21]. This corresponds to the ratio between the variance of the field photon number and the variance of a poissonian distribution with an equal first order momentum. We recognize four main situations:

- $f = 0$: Sub – poissonian light (Fock State)
- $f < 1$: Sub – Poissonian light (photonpairs, etc) (2.30)
- $f = 1$: Poissonian light (coherent laser source)
- $f > 1$: Super – Poissonian light

with f being:

$$f = \frac{\langle \Delta n^2 \rangle}{\langle n \rangle_{Poissonian}} \quad (2.31)$$

Thus, a single photon source would be clearly identified by a sub-poissonian statistics (in the ideal case with null Fano factor). The photon statistics of a field can be experimentally determined through a detection process; that means the photon flux must be tracked by a photodetector unit and converted into a signal from which the field statistical parameters can be calculated. In the section below, a brief description of this process is given.

2.2 The Photon Detection Process

A photodetector is an element that converts incident EM-radiation into a certain signal or information. A very basic example would be a semiconductor material in which the external light generates a photocurrent, that is subsequently amplified and correlated to the incoming photon stream intensity. Describing the field as:

$$\begin{aligned} \hat{E}(\mathbf{r}, t) &= -i \sum_k \sqrt{\frac{\hbar\omega_k}{2\varepsilon_0}} [\hat{a}_k(t) u_k(\mathbf{r}) + \hat{a}_k^\dagger(t) u_k^*(\mathbf{r})] = \\ &= \hat{E}^+(\mathbf{r}, t) + \hat{E}^-(\mathbf{r}, t) \end{aligned} \quad (2.32)$$

it can be shown that the detection probability is proportional to the probability of the incoming light to induce a certain transition in a quantum system representing the detector, the most simple of these being i.e. a two-level atom. If one had detectors with sufficiently low time response, jitter effects and high sensitivity, it would be possible to determine the statistical properties of a radiation by simply measuring the arrival times of the photons. However, this may present often some practical problems. Therefore, a setup that measures the field time correlation functions could perform the task in a more stable way, and the photon emission statistics would be therefore obtained from the interpretation of the Glauber functions. The first order Glauber correlation function is defined as:

$$g^{(1)}(\mathbf{r}_1, t_1; \mathbf{r}_2, t_2) = \frac{\langle \hat{E}^-(\mathbf{r}_1, t_1) \hat{E}^+(\mathbf{r}_2, t_2) \rangle}{\left(\langle \hat{E}^-(\mathbf{r}_1, t_1) \hat{E}^+(\mathbf{r}_1, t_1) \rangle \langle \hat{E}^-(\mathbf{r}_2, t_2) \hat{E}^+(\mathbf{r}_2, t_2) \rangle \right)^{\frac{1}{2}}} \quad (2.33)$$

It expresses the coherence properties, so the probability of having a constructive or destructive interference effect, of the EM radiation either on the temporal scale or the spatial scale by normalizing the correlated electric field amplitudes. Further knowledge can be acquired through higher-order functions, like the second one. This can be derived from the joint probability of having photon counting events at two different detectors, after the incident beam passes through a 50/50 beamsplitter:

$$p_{12} \propto \langle \hat{E}^-(\mathbf{r}_1, t_1) \hat{E}^-(\mathbf{r}_2, t_2) \hat{E}^+(\mathbf{r}_1, t_1) \hat{E}^+(\mathbf{r}_2, t_2) \rangle \quad (2.34)$$

The second order Glauber $g^{(2)}$ function correlates therefore the fields on the intensity scale, as it is shown below:

$$g^{(2)}(\mathbf{r}_1, t_1; \mathbf{r}_2, t_2) = \frac{\langle \hat{E}^-(\mathbf{r}_1, t_1) \hat{E}^-(\mathbf{r}_2, t_2) \hat{E}^+(\mathbf{r}_1, t_1) \hat{E}^+(\mathbf{r}_2, t_2) \rangle}{\left(\langle \hat{E}^-(\mathbf{r}_1, t_1) \hat{E}^+(\mathbf{r}_1, t_1) \rangle \langle \hat{E}^-(\mathbf{r}_2, t_2) \hat{E}^+(\mathbf{r}_2, t_2) \rangle \right)} \quad (2.35)$$

The previous expression can be rewritten in terms of the annihilation and creation operators. Assuming that $t_2 > t_1$, we can set $t_1 = t$ and $t_2 = t_1 + \tau$, with $\tau = t_2 - t_1$. Thus, the $g^{(2)}$ function can be expressed in function of

τ , and if we drop the notation for the spatial term (i.e. if dealing with a stationary mode) and set $t = 0$, it results:

$$g^{(2)}(\tau) = \frac{\langle \hat{a}^\dagger(0) \hat{a}^\dagger(\tau) \hat{a}(\tau) \hat{a}(0) \rangle}{\langle \hat{a}^\dagger(0) \hat{a}(0) \rangle^2} \quad (2.36)$$

or, in other terms:

$$g^{(2)}(\tau) = \frac{\langle \hat{I}(0) \hat{I}(\tau) \rangle}{\langle \hat{I}(0) \rangle^2} \quad (2.37)$$

It is possible to simulate the $g^{(2)}(\tau)$ function behaviour with the previously introduced three light distributions:

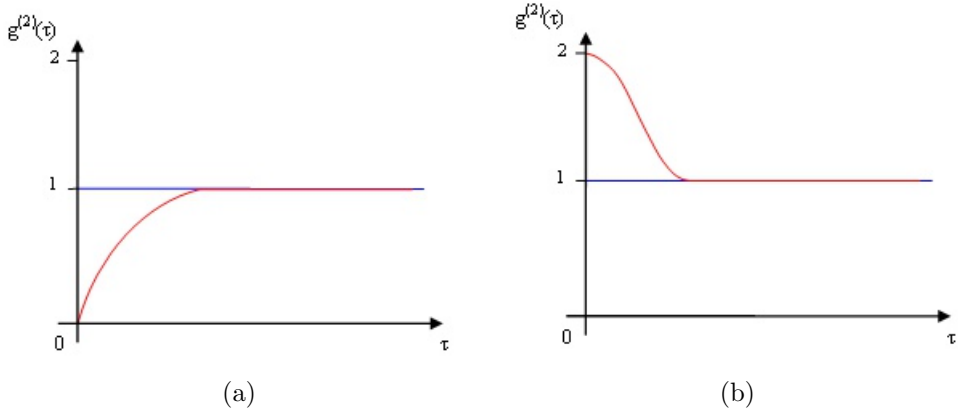


Figure 2.3: Second order correlation functions calculated for (a) subpoissonian and (b) superpoissonian light sources (depicted with red lines); the blue lines identify the poissonian statistics, typical i.e. for a coherent laser source. These functions can be used to obtain information on the light intensity fluctuations: photons generated by a thermal (superpoissonian) source will be detected in bunches, while the ones from a poissonian source are randomly distributed in time. A single photon source produces one photon per pulse, hence has lower variance in the photon number than the previous ones

At zero delay, the expression can be additionally simplified in:

$$g^{(2)}(0) = \frac{\langle \hat{N}^2 \rangle - \langle \hat{N} \rangle^2}{\langle \hat{N} \rangle^2} \quad (2.38)$$

where \hat{N} is the standard photon number operator. This form of second order correlation function can be quite useful for the characterization of the field

statistics; in case of thermal light, for example, we have that:

$$\begin{aligned} g^{(2)}(0) &= \frac{\langle \hat{N}^2 \rangle - \langle \hat{N} \rangle}{\langle \hat{N} \rangle^2} = \\ &= \left[1 - e^{-\frac{\hbar\omega}{k_b T}} \right] \frac{\text{Tr} \left[\sum_{n=0}^{n=\infty} e^{-\frac{\hbar\omega n}{k_b T}} |n\rangle \langle n| (\hat{N}^2 - \hat{N}) \right]}{\left(\text{Tr} \left[\sum_{n=0}^{n=\infty} e^{-\frac{\hbar\omega n}{k_b T}} |n\rangle \langle n| \hat{N} \right] \right)^2} = 2 \end{aligned} \quad (2.39)$$

while, for poissonian light:

$$g^{(2)}(0) = \frac{\langle \hat{N}^2 \rangle - \langle \hat{N} \rangle}{\langle \hat{N} \rangle^2} = \frac{|\alpha|^4}{|\alpha|^4} = 1 \quad (2.40)$$

And for a sub-poissonian Fock field:

$$g^{(2)}(0) = \frac{\langle \hat{N}^2 \rangle - \langle \hat{N} \rangle}{\langle \hat{N} \rangle^2} = 0 \quad (2.41)$$

It would be now useful to see how the $g^{(2)}(\tau)$ functions is linked to the physical reality. From (2.37), (2.36) and (2.40), we can see that, having a detection event at $t = 0$, the probability of having another one at $t = \tau$ is constant and equal for every τ if the light has poissonian statistics. So, the photons exit from the source at independent and random time intervals (perfect coherence). Having $g^{(2)}(\tau) > 1$ corresponds to a physical picture in which the probability of a photon detection event at $t = \tau$ when already one occurred at $t = 0$ is higher than the case of randomly emitted photons. Therefore, such light is said to be *bunched*, that means that photons have an enhanced probability to be generated simultaneously or ‘clustered’ together within short timescales (above, the $g^{(2)}$ function tends to a poissonian form). Thermal radiation shows indeed this feature. Finally, $g^{(2)}(\tau) < 1$ means that the joint probability of having a photon detected at $t = \tau$ after one realevated at $t = 0$ is lower than the probability of having two totally independent photon detection events. The physical situation corresponds

to a stream of photons separated in time by a minimum quantity τ_c . The second order correlation function shows therefore a characteristic dip for $\tau < \tau_c$. Single photon sources are identified by this feature, and the experimental setup one needs to determine such behaviour comes from the work of Hanbury, Brown and Twiss.

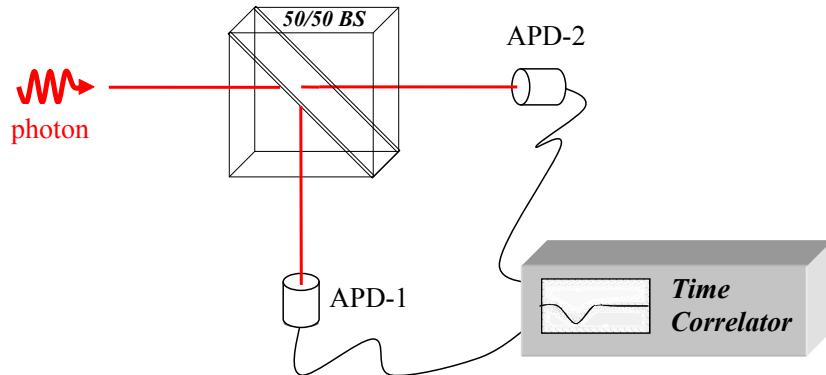


Figure 2.4: A standard Hanbury-Brown-Twiss setup used to calculate the autocorrelation function of an electromagnetic field. In a simple particle picture view, a beamsplitter splits the incoming photons in two directions, terminating each with an APD detector. The intensity at the two detectors is recorded (in function of the photon arrival times) and then computed as in (2.37). When dealing with a flux of single photons, each of them is splitted with a certain probability in two directions, with one APD detecting the particle. That means, that the intensity on the other is null, and at zero delay the $g^{(2)}(\tau)$ function goes to zero.

The HBT scheme plays a fundamental role in the realization of a photon correlation-interferometric method used to reveal the Nitrogen-Vacancy defects as solid-state single Fock-photon sources and to characterize their spectral behaviour.

Chapter 3

Solid State Single Photon Sources

3.1 Colour Centers in Wide Bandgap Materials

Wide bandgap materials are semiconductors or insulators with an electronic band significantly larger than 1.4 eV (namely the parameter for Gallium Arsenide, while for Silicon the value is 1.1eV). They have been extensively investigated for different applications, especially within the electronic and opto-electronic field, where they can be found in devices like LEDs, high-temperature transistors, sensors, etc. Recently, the demand of solid-state single photon sources for QIP has opened a new direction in the studying of these crystalline systems. In fact, what makes them so interesting for this purpose is the availability of specific chemically-stable defect centers, that are single or multiple lattice vacancies or impurities in the material, where the latter can be found in substitutional positions, so on lattice sites, or in interstitial regions. Some of these defects show an electronic configuration for which the ground and first excited levels are located within the bandgap [22]. The radiative transitions among them lead to photon emission that, if the centers have a sufficient concentration, might give to the whole crystal a characteristic colour. When the defects are independent, distinguishable and unclustered they can be seen as two or three-level isolated systems on which specific electronic transitions can be driven through photo-excitation.

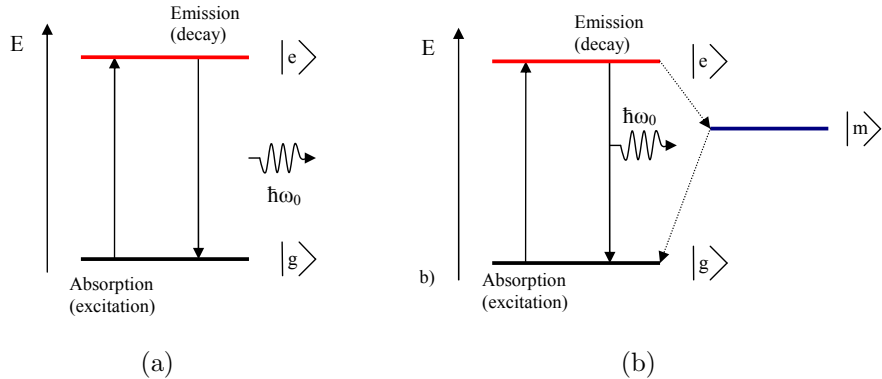


Figure 3.1: Simple schemes for a two level system (a) and a three level system (b). Ground states are identified by $|g\rangle$, upper excited states by $|e\rangle$. An ideal single photon source shall behave as (a), but systems as (b) are more diffuse. In that case, $|m\rangle$ is a third level which is often a metastable state.

Since the application of a proper incident radiation brings the defect into an excited state, other processes are subsequently triggered. A radiative decay, if involves the appropriate electron eigenstates, can lead to the emission of a single photon per pumping cycle and the system reset in a ground state. This particular property gathered lot of attention from the QIP sector, as it can be clearly used to produce the single photons on-demand that the linear optics quantum computer requires. But indistinguishability is an important requirement; the decoupling of the defect energy levels from the surrounding chemical species, and the lattice quality are two main parameters on which the emission linewidth depends. Furthermore, an ideal colour center shall display additional features in order to be exploited as source of identical single photons [23]. These are:

1. Photostable emission, free from bleaching or blinking
2. Short excited lifetime (and therefore, high photon generation rate)
3. No metastable or dark states
4. Weak electron-phonon coupling for a chosen electronic transition (in order to have most of the light emitted in the ZPL).
5. Zero-Phonon-Linewidth down to the fourier transform limit, in order to produce frequency-indistinguishable photons

Diamond is among the most promising materials for QIP applications. More than 500 light-emitting defects have been found in it [24], with the nitrogen-vacancy center focusing most of the attention on itself, for its relative brightness and stability even at high temperatures [25,26]. In the next paragraphs, its features will be discussed, with a particular insight on its optical properties.

3.2 Diamond Structure and General Properties

The diamond is a well-known allotropic form of Carbon, which is naturally available on the Earth from carbon-rich matter exposed for long times to high pressure conditions (4.5 GPa to 6GPa) and temperature (900 C to 1300 C), conditions that can be found in stable litospheric mantles. Artificially, it can be produced via different processes, where the most interesting are:

1. High Pressure High Temperature generation
2. Chemical Vapour Deposition

The diamond is characterized by a specific structure, consisting of a face-centered cubic lattice, with a bi-atomic basis where the first and second positions are identified by the primitive vectors $(0, 0, 0)$, $(\frac{1}{4}, \frac{1}{4}, \frac{1}{4})$. The average lattice constant is $a_0 = 3,67\text{\AA}$ and the atom density is $1,77 \times 10^{23} \text{at}/\text{cm}^3$. Ideally, the only element that makes up diamond is carbon; however, according to the formation conditions, different sorts of impurities are present. In the next section, a standard classification is presented.

3.3 Diamond Classification

A general method for categorizing diamonds uses the Nitrogen concentration in the specimen as first parameter [27]. Nitrogen, along with Boron, is the most common impurity that can be found within diamond structures. It can assume either interstitial or lattice positions, as also clusterize in different aggregates. Other common extrinsic defects are Boron, Silicon, Phosphor

[quote]. When Nitrogen is above 5 ppm, the diamond is said to be of type I. Otherwise, when $[N] < 5$ ppm it is considered as type II.

Type I Type Ia diamonds are characterized by having the Nitrogen impurities distributed over aggregates rather than in isolated lattice positions, with a concentration up to 3000 ppm. The minimal cluster unit consists of two Nitrogen atoms in adjacent sites, with each pair being separated from other ones. When Nitrogens are arranged in separated couples, the diamond is classified as being of type IaA. Another common impurity configuration consists of four Nitrogen atoms surrounding a vacancy; in such case, the diamond is of type IaB. On the other side, when the impurities are spread among the lattice with no continuity, the diamond is said to be of type Ib, with $5 < [N] < 500$. Other existing allotropic forms are excluded from the common type classification.

Type II Type II diamond shows a Nitrogen concentration below 5 ppm. Specimen with impurity concentrations in the range of ppb, including N atoms, are said to be of type IIa. Nevertheless, when Boron is present in order of hundreds of ppbs, but Nitrogen is not, the diamond is classified as type IIb.

3.4 The Nitrogen-Vacancy Center Structure

The Nitrogen-vacancy center is a point defect consisting in a substitutional Nitrogen atom, located on a lattice site, and an adjacent reticular carbon vacancy. The overall structure has trigonal symmetry and transforms according to the irreducible representations of the C_{3v} group [28]. The NV center has three main symmetry axes, and an equal number of reflection planes.

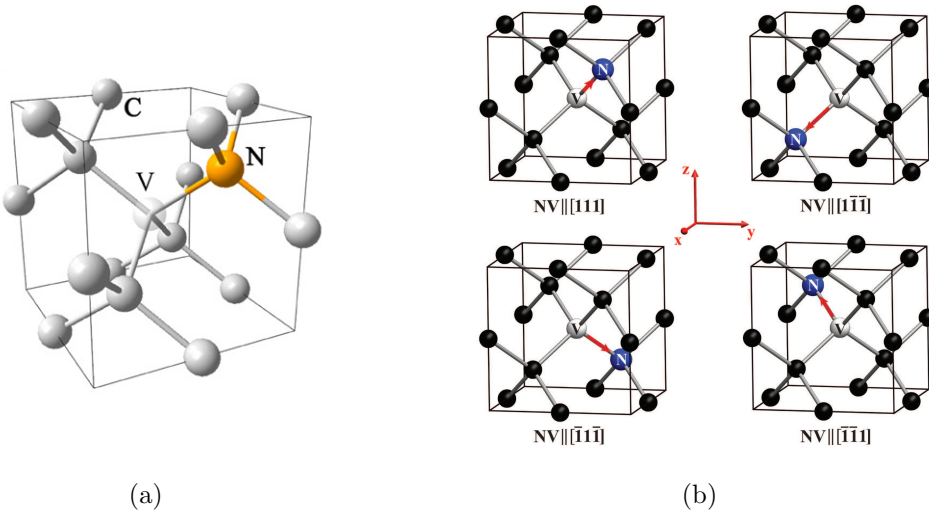


Figure 3.2: Image (a) depicts the Nitrogen Vacancy center in the diamond lattice, showing the position of N, C and the vacancy; (b) illustrates the four possible equivalent crystallographic axes. Images courtesy of [Aharonovic,Acosta].

The vector connecting the impurity with the vacancy can lie along four possible [29] crystallographic axes: $[1\bar{1}\bar{1}]$, $[111]$, $[\bar{1}\bar{1}\bar{1}]$, $[\bar{1}1\bar{1}]$. However, as they are equivalent respect to the color center properties, from this point we will assume the $[111]$ orientation. According to the current models, the defect center is found in two main charge states [30]: the NV^0 and the negatively charged NV^- . The first has five active electrons, three from the first-neighbour carbon dangling bonds and two from the nitrogen atom; the NV^- has the same latter configuration with one more electron, captured from the crystal. In this work only the last type of nitrogen-vacancy will be taken in account; for semplicity the negative sign will be omitted. A modelization of the color center orbital wavefunctions was successfully performed with different approaches [31,32,33]. According to the model reported in [32], three sp^3 carbon orbitals (labeled generally as a , b , c), pointing toward the vacancy (tetrahedrally coordinated dangling bonds) and one nitrogen sp^3 orbital (labeled d) can be linearly combined to obtain four single-electron orthonormal wavefunctions:

$$e_x = \frac{(2ca - b)}{\sqrt{6 - 6S}} \quad (3.1a)$$

$$e_y = \frac{(a - b)}{\sqrt{2 - 2S}} \quad (3.1b)$$

$$u = d - \lambda v \quad (3.1c)$$

$$v = \frac{a + b + c}{\sqrt{3 - 6S}} \quad (3.1d)$$

It must be noticed that X, Y and Z refer in this case to new coordinates oriented as depicted in Fig. 3.3. The S and λ overlap integrals are defined as:

$$S = \langle a | b \rangle \quad (3.2a)$$

$$\lambda = \langle d | v \rangle \quad (3.2b)$$

The set of orbitals transforms according to different irreducible representations of the C_3v group; u and v are totalsymmetric while e_x and e_y follow the conditions for E_x and E_y (that is, E representation on X and Y basis). They can be also qualitatively ordered in terms of associated energy eigenstates by applying general principles, as charge distribution and simmetry features. The resulting distribution is:

$$u < v < e_x = e_y \quad (3.3)$$

where e_x and e_y are degenerate; u is localized near the nitrogen atom, v between the nuclei of the whole center. It is proven via ESR measurements that most of the charge density lies however on the first-neighbour carbon atoms. According to Hund rules, ground states are supposed to be in form of $u^2v^2e^2$, with the u and v orbital-singlets totally occupied and the e doublet having two electrons. On the other side, the first excited states can be, in a simple single-particle picture, $u^2v^1e^3$; that means with one electron transferred from the v orbital to the e orbital. Fig. 3.3 points the dispositions:

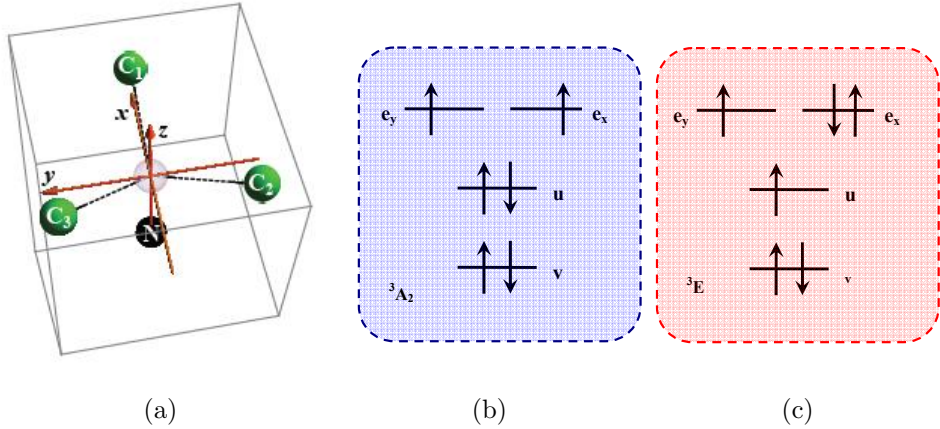


Figure 3.3: In (a), the NV center coordinate system is depicted; (b) and (c) point out the electronic disposition among the orbitals for the excited and ground states.

For the ground state with upper shell e^2 , there are four possible single-particle spin-orbit configurations; since two electrons are available, the possible spatial wavefunctions would show:

$$e \otimes e = A_1 \oplus A_2 \oplus E \quad (3.4)$$

and they would therefore span three symmetry representations: A₁, A₂ and E. Now, multi-electron states can be calculated by constructing wavefunctions by combining Slater determinants of single-electron spin-orbit products that are eigenstates of the total spin number operator \hat{S} . The compliance to the Pauli principle is assured by the fact that, among the manifold states obtained, only those eigenstates of the anti-symmetrizing operator are selected. The overall procedure is formalized from [32,33] as:

$$|\bar{a}..r\rangle = \frac{1}{\sqrt{N!}} \begin{vmatrix} a(1)\alpha(1) & \dots & a(N)\alpha(N) \\ b(1)\beta(1) & \dots & b(N)\beta(N) \\ \dots & \dots & \dots \\ r(1)\alpha(1) & & r(N)\alpha(N) \end{vmatrix} \quad (3.5)$$

$$|\bar{a}..r\rangle = \frac{1}{\sqrt{N!}} \sum_P (-1)^{\Theta(P)} \times [a(1)\alpha(1)b(2)\beta(2)...r(N)\alpha(N)]_P \quad (3.6)$$

where $\alpha()$ are the spin up/down basis states, and $a()$ represent the spatial orbital functions. In order to give a more compact notation, the projected

spin quantum number will be included in the orbital symbol as a overlying bar (which indicates $m_s = -1/2$, while its absence specifies that $m_s = 1/2$). The calculated spin eigenstates functions are:

Configuration	Γ	g	Wave function ($m=S$)
$u^2v^2e^2$	1A_1	1	$\frac{1}{\sqrt{2}}[u\bar{u}\nu\bar{v}e_X\bar{e}_X\rangle+ u\bar{u}\nu\bar{v}e_Y\bar{e}_Y\rangle]$
	3A_2	3	$ u\bar{u}\nu\bar{v}e_Xe_Y\rangle$
	1E	2	$\frac{1}{\sqrt{2}}[u\bar{u}\nu\bar{v}e_X\bar{e}_X\rangle- u\bar{u}\nu\bar{v}e_Y\bar{e}_Y\rangle],$ $\frac{1}{\sqrt{2}}[u\bar{u}\nu\bar{v}e_X\bar{e}_Y\rangle+ u\bar{u}\nu\bar{v}e_Y\bar{e}_X\rangle]$
u^2ve^3	1E	2	$\frac{1}{\sqrt{2}}[u\bar{u}\nu\bar{v}e_Xe_Y\bar{e}_Y\rangle- u\bar{u}\nu\bar{v}e_Xe_Y\bar{e}_Y\rangle],$ $\frac{1}{\sqrt{2}}[u\bar{u}\nu\bar{v}e_Ye_X\bar{e}_X\rangle- u\bar{u}\nu\bar{v}e_Ye_X\bar{e}_X\rangle]$
	3E	1	$ u\bar{u}\nu e_Xe_Y\bar{e}_Y\rangle, u\bar{u}\nu e_Ye_X\bar{e}_X\rangle$
$u\nu^2e^3$	1E	2	$\frac{1}{\sqrt{2}}[u\nu\bar{\nu}\bar{e}_Xe_Y\bar{e}_Y\rangle- \bar{u}\nu\bar{\nu}e_Ye_X\bar{e}_Y\rangle],$ $\frac{1}{\sqrt{2}}[u\nu\bar{\nu}\bar{e}_Ye_X\bar{e}_X\rangle- \bar{u}\nu\bar{\nu}e_Ye_X\bar{e}_X\rangle]$
	3E	1	$ u\nu\bar{\nu}\bar{e}_Xe_Y\bar{e}_Y\rangle, u\nu\bar{\nu}\bar{e}_Ye_X\bar{e}_X\rangle$

Table 3.1: Spin eigenfunctions of highest total spin number according to [x]

Total wavefunctions are obtained by combining the total spin number eigenstates with orbital states (eigenfunctions of the total orbital angular momentum operator \hat{L}), as done in the case of weak L-S coupling. Therefore is important that the overall antisymmetry is preserved and that the results are chosen among those that transform according to the group operations of the colour center. By satisfying these conditions, it can be proven that the obtained expressions are eigenfunctions both of the total orbital angular momentum operator and total spin operator. Consequently, the ground states can be identified as those that maximize the total spin number S in $u^2v^2e^2$ configuration. Thus, including spin-spin and spin-orbit couplings,

they are triplets of the form:

$$|\psi_{E_x}^{g,so}\rangle = -\frac{1}{\sqrt{2}}(|u\bar{u}v\bar{v}\bar{e}_x\bar{e}_y\rangle - |u\bar{u}v\bar{v}e_xe_y\rangle) \quad (3.7a)$$

$$|\psi_{E_y}^{g,so}\rangle = -\frac{i}{\sqrt{2}}(|u\bar{u}v\bar{v}e_xe_y\rangle + |u\bar{u}v\bar{v}\bar{e}_x\bar{e}_y\rangle) \quad (3.7b)$$

There is one totalsymmetric configuration (A_1) and two more degenerate functions of E symmetry. Without an external magnetic field, these states are degenerate in energy and the spin orbit coupling is negligible. Their symmetry properties, excluding fine structure, are 3A_2 , and they are identified as the NV center ground states. With the same procedure, the most relevant spin-orbit excited states (that in absence of coupling transform as 3E) are:

$$\begin{aligned} |\psi_{E_x}^{e,so}\rangle = & -\frac{1}{2}[i(|u\bar{u}ve_xe_y\bar{e}_y\rangle + |u\bar{u}\bar{v}\bar{e}_xe_y\bar{e}_y\rangle) \\ & + (|u\bar{u}\bar{v}e_x\bar{e}_x\bar{e}_y\rangle - |u\bar{u}ve_x\bar{e}_x\bar{e}_y\rangle)] \end{aligned} \quad (3.8a)$$

$$\begin{aligned} |\psi_{E_y}^{e,so}\rangle = & \frac{1}{2}[i(|u\bar{u}ve_x\bar{e}_xe_y\rangle + |u\bar{u}\bar{v}e_xe_x\bar{e}_y\rangle) \\ & - (|u\bar{u}\bar{v}\bar{e}_xe_y\bar{e}_y\rangle - |u\bar{u}ve_xe_y\bar{e}_y\rangle)] \end{aligned} \quad (3.8b)$$

$$|\psi_{E'_x}^{e,so}\rangle = -\frac{1}{\sqrt{2}}(|u\bar{u}v\bar{e}_x\bar{e}_xe_y\rangle + |u\bar{u}\bar{v}\bar{e}_x\bar{e}_xe_y\rangle) \quad (3.8c)$$

$$|\psi_{E'_y}^{e,so}\rangle = \frac{1}{\sqrt{2}}(|u\bar{u}v\bar{e}_x\bar{e}_y\bar{e}_y\rangle + |u\bar{u}\bar{v}\bar{e}_x\bar{e}_xe_y\rangle) \quad (3.8d)$$

$$\begin{aligned} |\psi_{A_2}^{e,so}\rangle = & \frac{1}{2}[(|u\bar{u}\bar{v}\bar{e}_xe_x\bar{e}_y\rangle - |u\bar{u}ve_xe_y\bar{e}_y\rangle) \\ & - i(|u\bar{u}ve_x\bar{e}_xe_y\rangle + |u\bar{u}\bar{v}e_x\bar{e}_x\bar{e}_y\rangle)] \end{aligned} \quad (3.8e)$$

$$\begin{aligned} |\psi_{A_1}^{e,so}\rangle = & \frac{1}{2}[-i(|u\bar{u}\bar{v}\bar{e}_xe_x\bar{e}_y\rangle - |u\bar{u}ve_xe_y\bar{e}_y\rangle) \\ & + (-|u\bar{u}ve_x\bar{e}_xe_y\rangle + |u\bar{u}\bar{v}e_x\bar{e}_x\bar{e}_y\rangle)] \end{aligned} \quad (3.8f)$$

Despite spin-orbit coupling can give total excited-state wavefunctions of A_1 and A_2 symmetry, no orbitals transforming as those IRREPs are allowed with $u^2v^1e^3$ configuration, due to incompatibility with the Pauli exclusion principle. Since until now only triplet states were described, it must be

noted that experimental evidences prove that at least one singlet state (arising from the $u^2v^2e^2$ electronic configuration) lies within the bandgap [38]: the theory is able to predict it and two more of the form:

$$\left| \psi_{A_1}^{i,so} \right\rangle = \frac{1}{\sqrt{2}} (\left| u\bar{u}v\bar{v}e_x\bar{e}_x \right\rangle + \left| u\bar{u}v\bar{v}e_y\bar{e}_y \right\rangle) \quad (3.9a)$$

$$\left| \psi_{E_x}^{i,so} \right\rangle = \frac{1}{\sqrt{2}} (\left| u\bar{u}v\bar{v}e_x\bar{e}_x \right\rangle - \left| u\bar{u}v\bar{v}e_y\bar{e}_y \right\rangle) \quad (3.9b)$$

$$\left| \psi_{E_y}^{i,so} \right\rangle = \frac{1}{\sqrt{2}} (\left| u\bar{u}v\bar{v}\bar{e}_xe_y \right\rangle - \left| u\bar{u}v\bar{v}e_x\bar{e}_y \right\rangle) \quad (3.9c)$$

with A_1 being identified as a *metastable* state of the NV center, and the 1E_1 doublet coming only recently under investigation [36,37,43, 48]. In the next section, an energy estimation for the wavefunctions previously introduced will be given.

3.5 Energy Levels of the NV Center

Energy levels of the NV ground and excited states can be obtained via calculation of an electron Hamiltonian operator eigenvalues [31,33]:

$$H_e = H_0 + H_{so} + H_{ss} \quad (3.10)$$

Where H_0 accounts for the electron kinetic energy and Coulomb interactions, H_{so} accounts for the spin-orbit coupling, H_{ss} for the electron spin-spin coupling. Concerning the ground states, the spin-orbit interaction can be neglected, while the spin-spin coupling must be considered with the expression:

$$H_{ss} = \frac{\mu_0 g_e \mu_B^2}{4\pi\hbar^2} \sum_{i>j} \frac{\mathbf{s}_i \cdot \mathbf{s}_j}{|\mathbf{r}_{ij}|^3} - \frac{3(\mathbf{s}_i \cdot \mathbf{r}_{ij})(\mathbf{s}_j \cdot \mathbf{r}_{ij})}{|\mathbf{r}_{ij}|^5} \quad (3.11)$$

with \mathbf{s}_i , \mathbf{p}_i , \mathbf{r}_i representing the spin, momentum and positions of the i -th electron, g_e its free g-factor and μ_0 the Bohr magneton. The spin-orbit coupling Hamiltonian, important for the excited states, has instead the form:

$$H_{so} = \frac{1}{2m^2c^2} \sum_i \nabla V_{Ne}(\mathbf{r}_i) \times \mathbf{p}_i \cdot \mathbf{s}_i \quad (3.12)$$

Here, V_{Ne} is a nucleus-electron potential. In absence of strain, external electric or magnetic fields, and neglecting the hyperfine structure that arises from the interaction between nuclear magnetic dipole moments and electron spins, the energy level diagram for the ground and first NV excited states is: Where the spin-orbit symmetry is pointed on the right. It is theoret-

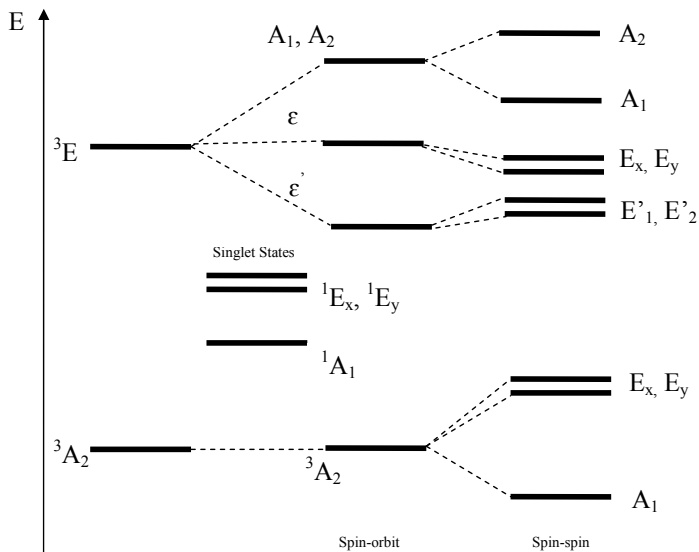


Figure 3.4: Nitrogen-Vacancy energy levels (according to [50]) are depicted in the case of spin-orbit and spin-spin couplings.

ically and experimentally confirmed that both the triplets 3E and 3A_2 , as also the spin-singlet 1A lie within the diamond bandgap [34]; they confer most of the nitrogen-vacancies optical and magnetic properties. The effect of external perturbations, such as strain or electric/magnetic potentials, might be included by adding the specific terms in the Hamiltonian (3.10). Remembering that ξ represents the strain tensor, this means:

$$H_{\text{strain}} = \sum_i (\mathbf{e} \mathbf{r}_i) \cdot \boldsymbol{\xi} \quad (3.13)$$

and leads to an energy shift of NV center levels. External electric and magnetic forces \mathbf{E}, \mathbf{B} are included via Stark and Zeeman couplings of the

form:

$$H_{\text{stark}} = \sum_i (e\mathbf{r}_i) \cdot \mathbf{E} \quad (3.14a)$$

$$H_{\text{zeeman}} = \sum_i (\mathbf{r}_i \times \mathbf{p}_i + g_e \mathbf{s}_i) \cdot \mathbf{B} \quad (3.14b)$$

which results also in energy shifts and removing of degeneracy between 3A_2 states and excited orbital-doublets. The combination and effect of these two phenomena will be a fundamental topic in the NV emission linewidth theoretical description. At low temperatures, lattice strain is generally not considered as a relevant broadening factor, as it induces static energy splitting within the excited states; dynamic Jahn-Teller effect [44] appears, due to second order phonon coupling with the two-level system, at temperatures higher than 20K. Nevertheless a dynamic electric force can induce a considerable dynamic energy shift of the NV levels, making the eventual radiative transitions among them generate distinguishable photons, unfit for QIP applications. In chapter 4 these details will be extensively discussed.

3.6 Optical Transitions: Selection Rules and Spectra

Optical transitions among the NV center levels are dipole allowed if the dipole matrix elements are nonzero:

$$\langle \psi_i | e\mathbf{r} \cdot \zeta | \psi_f \rangle \neq 0 \quad (3.15)$$

where ψ_f is the final state, ψ_i the initial, $e\mathbf{r}$ the dipole operator and ζ the polarization of the absorbed or emitted photon. It can be noticed that the non-zero condition on (3.15) is satisfied primarily when the ψ_i and ψ_f functions have different orbital parts, i.e. if they are respectively of the form $u^2v^2e^2$ and $u^2v^1e^3$. Symmetry properties of the different wavefunctions involved can be used to determine the transition dipole moment. Specifically, the main condition tell us that the (3.15) elements must belong to the

totalsymmetric A_1 irreducible representation of the C_3v group. Another requirement for having non-null transition probability is that the total spin number S and its z -projection m_s have to be conserved. However, spin-orbit coupling might relax this rule, which therefore has not to be considered as strict as the previous one. The scheme in Fig. 3.3 provides an intuitive picture of the allowed processes. The nitrogen-vacancy fluorescence spectra in

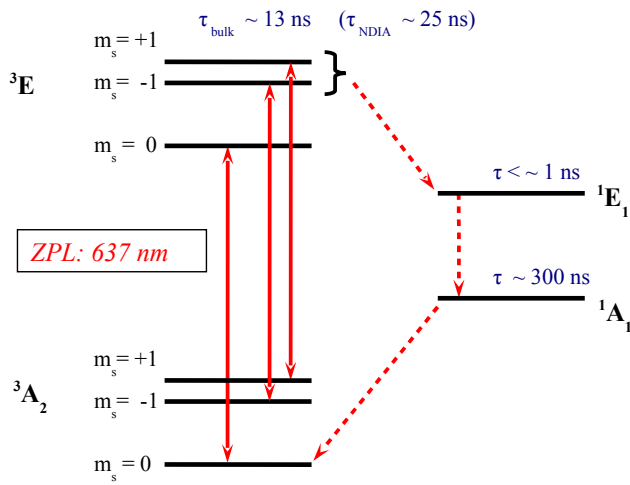


Figure 3.5: Simplified scheme of the allowed transitions between NV ground and excited states, with the lifetimes of the latter determined from [39, 43]. Singlet states that are involved in ISC processes and non-radiative decays are shown on the right [43].

the visible region arises from the radiative transitions between 3E levels and 3A_2 ground states, separated by 1.945 eV or 637nm. The involved dipole moments are oriented along the X and Y axes. When external fields are applied (i.e. under continuous off-resonant excitation center) a state recombination occurs, allowing even transitions with diagonal or elliptic dipoles in the X-Y plane. The experimental spectrum for off-resonant excitation at room temperature is shown below.

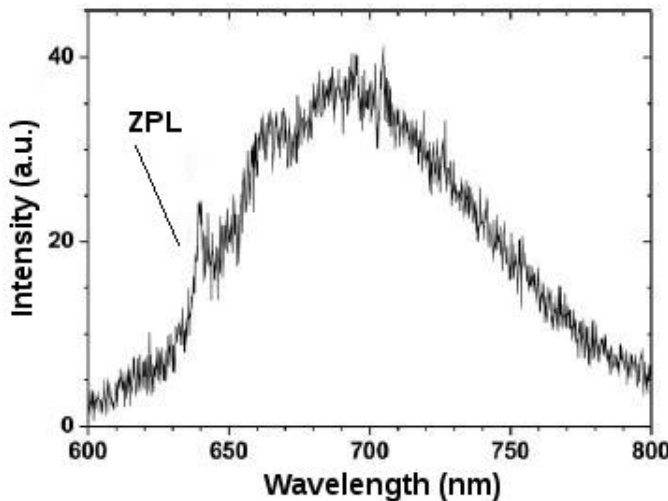


Figure 3.6: A Single Nitrogen-Vacancy fluorescence spectra taken under 532 nm CW-Laser excitation. At room temperature, the ZPL is almost completely covered by the broad phonon side bands

The broad signal in the [560, 800]nm interval - known as Phonon Side Bands (PSB) - stems mainly from the linear coupling between electrons and vibrational modes of the lattice. At room temperature, 95% to 97% of the ${}^3E \rightarrow {}^3A_2$ photons are emitted in this region. The Franck-Condon principle explains such fact by showing that the transitions between vibronic levels are more probable if the overlap of the excited and ground state coupled phonon wavefunctions is maximized.

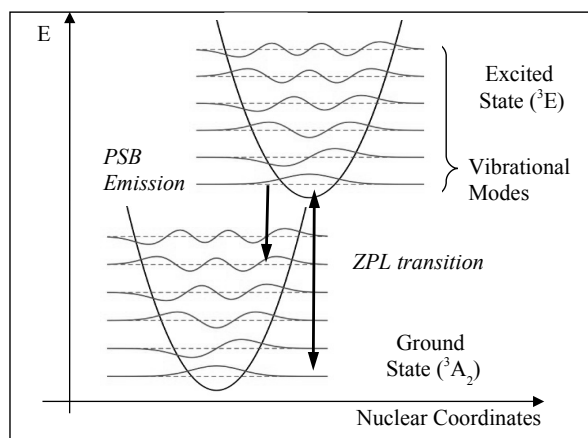


Figure 3.7: Illustration of the Franck-Condon principle. The probability for having a transition between two vibronic levels increases with the degree of overlap among their vibrational functions. Zero-phonon-line transitions become prominent if the high-energy phonons are suppressed.

In order to minimize the emission in PSB, it is necessary to work at very low temperatures in a way that reticular dynamics is minimized and transitions between lowest phonon energy levels of the electronic states become possible. Under such conditions, the emission spectra changes into the more convenient form shown in fig(3.7), where the $^3E \rightarrow ^3A_2$ transition occurs

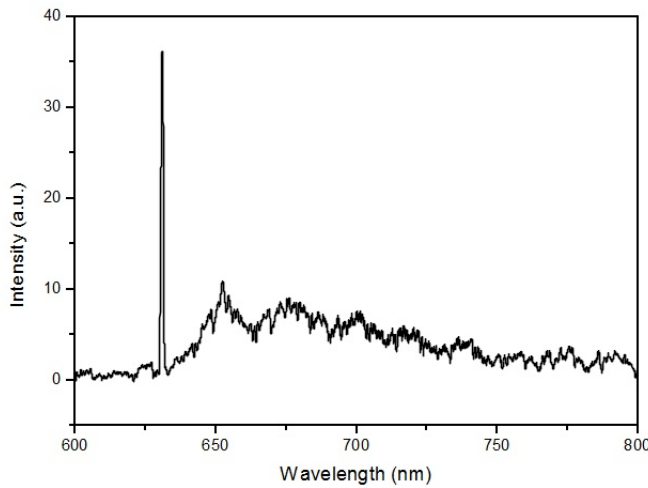


Figure 3.8: Low-temperature (5K) emission spectra of an NV-center under 532 CW Laser pumping. ZPL transitions are now clearly visible, due to the non-activation of high phonon quantas

primarily via zero-point lattice vibrational levels (Zero-Phonon-Line). According to Fig. 3.7, optical excitation might be performed either resonantly, so with 637nm light, or off-resonantly, so with the whole wavelengths between 480nm and 620 nm (out of this region, efficiency decreases rapidly). Standard setups implement usually 532nm green coherent light for the optical pumping of nitrogen vacancies. The lifetime of the 3E excited state is circa 12ns for NV centers in bulk diamond and it goes up to 25ns for centers in nanodiamonds (due to reticular strains and deformations that act on the wavefunction symmetries weakening the transition dipoles). Furthermore, a non-radiative decay channel is available from the excited triplet, that is through the 1E_1 and 1A_1 singlet states. The most accounted mechanism for such process is an ISC (intersystem crossing) between the 3E spin triplet states of $m_s = \pm 1$ and the 1E_1 spin singlets [43]. These decay subsequently to the 1A_1 level, which relaxes then in 300ns to the $3A_2$ ground state

having $m_s = 0$. Nevertheless, from the preferential involvement of excited states with nonzero spin arises the so-called optical polarization of the NV under non-resonant excitation [49]. Since non-resonant light permits all of the spin-conserving transitions in Fig. 3.5, but the ISC comes mainly from $m_s = \pm 1$ excited states, after a short time the NV will be polarized in the zero total spin ground state. It has to be remarked that with temperatures higher than 1K and no excitation, all of the ground state spin sublevels are in thermal equilibrium. The off-resonant excitation removes this population number degeneracy, bringing the center into the $^3A_2, m_s = 0$, ground state. However, fluorescence becomes higher when this process is in regime, because initial states with $m_s = 0$ will be transformed in excited states of $m_s = 0$, from which non-radiative decay is less probable. A way to remove the optical polarization is through a microwave radiation that recombines the spin-state populations within the 3A_2 orbitals. This feature can be used to implement electron spin-qubits in nitrogen-vacancies, that can be read by means of optically detected magnetic resonance. Details on this topic are given in [35, 38, 49], while an implementation of the electron spin manipulation in QIP is given in [41, 42, 47].

3.7 NV Centers in Nanodiamonds

Nitrogen-Vacancy centers can be also found in nanodiamonds, that are diamond particles with a submicrometric size, produced via detonation or milling of CVD growth diamond. The interest in them stems from the pos-

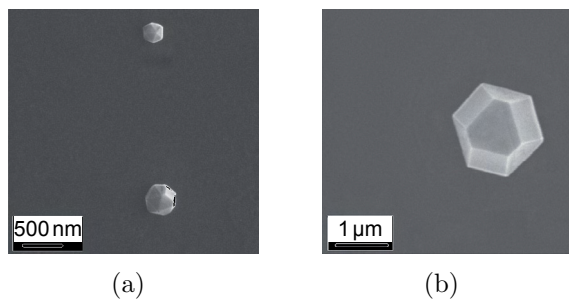


Figure 3.9: SEM images of nanodiamonds

sibility to couple such objects to photonic crystal structures, hence to couple

single photon emitters to wave-guides or other solid-state optical elements. Within this framework, a planar realization of a Hong-Ou-Mandel circuit has been proposed and based on a GaP photonic crystal with L3 cavities hosting single nanodiamonds, having thus one NV center for each. The other advantage in this case is also the enhancement of ZPL transitions via Purcell effect [40].

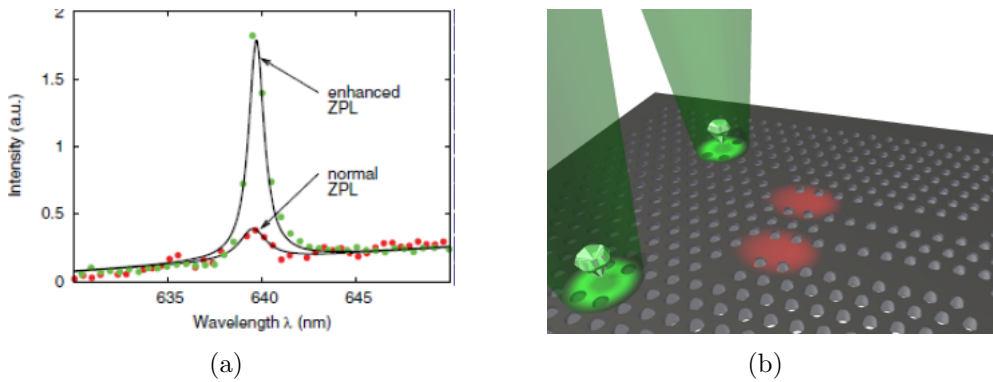


Figure 3.10: In the first graphic (a) the Purcell enhancement of NV centers ZPL in L3 photonic crystal cavities is shown [40]. In (b) a sketch of a possible planar circuit realizing maximally entangled (HOM) photon states.

Chapter 4

Line broadening in Photon Emitters

4.1 Two Level Systems and Single Photon Wavepackets

In the previous chapter, the Nitrogen-Vacancy center electronic structure and energy levels were introduced; in particular, we have pointed out that two orbitals lie within the diamond bandgap and can be considered as a two-level system, capable of generating single photons via radiative decay. From chapter 1, it is clear that these elementary particles must be identical to each other in order to be suitable for quantum optical gates. It is convenient to give a short and qualitative description of indistinguishability of photons. Namely, we consider two photons as identical when they are described by the same wave-packet with equal frequency spectra, same spatial-temporal mode and equal polarization. The latter property in NV centers radiation can be controlled by using linearly polarized light to excite specific dipoles of the point defect, as defined in the previous chapter, in order to obtain radiation emitted in the same polarization state. The frequency spectra is related to the emitting media and the emission process. Stepping back to the Nitrogen-Vacancy structure, it can be assumed that the radiative transitions ${}^3A_2 \rightarrow {}^3E$ are ideally obeying the selection rules $\Delta m_s = 0$ and $\Delta l = \pm 1$. For simplicity, spin-orbit and spin-spin

couplings for these levels are accounted as neglectable. Furthermore no external electric and magnetic fields, hyperfine interactions and lattice strains are active on the defect center. For a (physically unjustified) almost-infinite excited state lifetime, an emitted photon would correspond, in the QFT framework, to a non-localized monochromatic single-mode excitation of the quantum electromagnetic field; thus the spectral distribution would be a Dirac delta function. However, it is obvious that such picture is incorrect as an almost-infinite lifetime would imply no transitions at all, so that's the first effect to take account of. The wave-packet (or *pulse*) description for the emitted photon needs to be introduced as a direct consequence of this finiteness. Such wave-packets are related to the plane-wave modes described in Chapter 2 via the transformations introduced by Titulaer-Glauber[55]:

$$\Upsilon_{j,\xi}(\mathbf{x}, t) = i \left(\frac{\hbar c}{2\epsilon_0} \right)^{1/2} \int \frac{d^3 k}{2\pi^3} \sqrt{k} U_j^\xi(\mathbf{k}) \mathbf{u}_{\mathbf{k},\xi}(\mathbf{x}) e^{-i\omega_{\mathbf{k}} t} \quad (4.1)$$

where $\Upsilon_{j,\xi}(\mathbf{x}, t)$ is a photon wavepacket of average frequency j and polarization ξ , $\mathbf{u}_{\mathbf{k},\xi}$ are the monocromatic plane-waves defined in chapter 2 and U_f accounts for a unitary transformation matrix that respects the condition:

$$\sum_j U_j^\xi(\mathbf{k}')^* U_j^\xi(\mathbf{k}) = 2\pi^3 \delta(\mathbf{k}' - \mathbf{k}) \quad (4.2)$$

It has to be noticed that spatial-temporal wave-packet modes do not form an orthonormal set, as it can be seen evaluating their overlap integral through canonical scalar product:

$$\langle \Upsilon_{j,\xi} | \Upsilon_{m,\xi} \rangle = \int \Upsilon_{j,\xi}(\mathbf{x}, t)^* \Upsilon_{m,\xi}(\mathbf{x}, t) d^3 x = \quad (4.3a)$$

$$= \frac{\hbar c}{2\epsilon_0} \int \frac{d^3 k}{2\pi^3} k U_j^\xi(\mathbf{k})^* U_m^\xi(\mathbf{k}) \neq \delta_{k,m} \quad (4.3b)$$

This stems from the \sqrt{k} factor that weightens every frequency component [55]. Details about the construction of a new scalar product that overcomes this over-completeness are here unnecessary. An important concept to point out is instead the possibility to define through (4.1) new pulsed-mode cre-

ation and annihilation operators[55, 56]:

$$\hat{b}_{j,\xi} = \int \frac{d^3k}{8\pi^3} U_j^\xi(\mathbf{k}) \hat{a}_{\mathbf{k},\xi} \quad (4.4a)$$

$$\hat{b}_{j,\xi}^\dagger = \int \frac{d^3k}{8\pi^3} U_j^{\xi*}(\mathbf{k}) \hat{a}_{\mathbf{k},\xi}^\dagger \quad (4.4b)$$

that obey the bosonic commutation relations as the orthonormal plane-wave monochromatic modes. Fock states are generated as:

$$\hat{b}_{j,\xi}^\dagger |0\rangle = |1\rangle_{j,\xi} \quad (4.5)$$

Since the unitary transformation used in (4.2) is linked to a spectral amplitude function for the wave-packet, a more intelligible form of the (4.4) can be written in ω representation:

$$\hat{b}_{\chi,\xi}^\dagger = \int d\omega \chi_\xi^*(\omega) \hat{a}_\xi^\dagger(\omega) \quad (4.6a)$$

$$\hat{b}_{\chi,\xi} = \int d\omega \chi_\xi(\omega) \hat{a}_\xi(\omega) \quad (4.6b)$$

Where $\chi_\xi^{(\omega)}$ is a spectral distribution function. In our specific case we can obtain it by calculating the temporal evolution of the defect center system coupled to a continuum of photon modes. A relatively simple model can be set up by considering the emitter as a two-level quantum system made with a ground state $|g\rangle$ and an excited state $|e\rangle$ separated by energy ω_0 with only the dipole interaction with EM fields considered through the specific operator[17,57]:

$$\hat{\mu} = \mu |g\rangle \langle e| + \mu^* |e\rangle \langle g| \quad (4.7)$$

where the matrix elements are given as $\mu = \sum_j q_j \langle g | \hat{r}_j | e \rangle$. The total Hamiltonian for the coupled system would than be:

$$\hat{H} = \hbar\omega_0 (|e\rangle \langle e| - |g\rangle \langle g|) + \hbar\omega \left(\hat{a}^\dagger \hat{a} + \frac{1}{2} \right) - \hat{\mu} \cdot \hat{E}(r_0) \quad (4.8)$$

The last term accounts for the interaction part and in rotating-wave approximation is:

$$\hat{H}_{\text{int}} = i\mu \cdot E(r_0) [|e\rangle\langle g| \cdot \hat{a} e^{-i(\omega-\omega_0)t} - |g\rangle\langle e| \hat{a}^\dagger e^{i(\omega-\omega_0)t}] \quad (4.9)$$

With a multiplicity of radiation modes (knowing that g_k gives the coupling strength between the dipole transition in a photon emission) and the use of Pauli matrixes, the full Hamiltonian becomes:

$$\hat{H} = \left[\frac{\hbar\omega_0}{2} \right] \hat{\sigma}_z + \sum_k \hbar\omega_k \left(\hat{a}_k^\dagger \hat{a}_k + \frac{1}{2} \right) + i\hbar \sum_k g_k \left(\hat{\sigma}^+ \hat{a}_k - \hat{\sigma}^- \hat{a}_k^\dagger \right) \quad (4.10)$$

The Pauli matrices are:

$$\sigma_z = \begin{pmatrix} 1 & 0 \\ 0 & -1 \end{pmatrix} \quad \sigma^+ = \begin{pmatrix} 0 & 1 \\ 0 & 0 \end{pmatrix} \quad \sigma^- = \begin{pmatrix} 0 & 0 \\ 1 & 0 \end{pmatrix} \quad (4.11)$$

And the expanded coupling coefficient is:

$$g_k = \sqrt{\frac{\omega_k}{2\epsilon_0\hbar V}} \hat{\xi} \cdot \langle \psi_i | \hat{\mu} | \psi_f \rangle \quad (4.12)$$

Therefore, the solution of (4.10) can be written as as:

$$|\tilde{\psi}(t)\rangle = \tilde{r}(t) e^{-i\omega_0 t/2} |0\rangle_f |e\rangle + \sum_k \tilde{b}_k(t) e^{i\omega_0 t/2 - i\omega_k t} a_k^\dagger |0\rangle_f |g\rangle \quad (4.13)$$

where the light vacuum state is $|0\rangle_f = \prod_k |0\rangle_k$ and the Fock state $a_k^\dagger |0\rangle_f = |0\rangle_1 |0\rangle_2 \dots |1\rangle_k \dots |0\rangle_n$. The coefficients $\tilde{r}(t)$ and $\tilde{b}_k(t)$ describe respectively the time-varying amplitudes of excited and ground states entangled to zero and one photon in the space (with the latter being represented by a sum over different monochromatic single photon states as in the wave-packet picture). Through the Wigner-Weisskopf approach [38, 58], one may set up the dynamical equations that describe the time-evolution of the $r(t)$ and

$b(t)$ coefficients:

$$\frac{d\tilde{r}}{dt} = -i \sum_k g_k e^{i(\omega_0 - \omega_k)t} \tilde{b}_k \quad (4.14)$$

$$\frac{d\tilde{b}_k}{dt} = -ig_k e^{i(\omega_0 - \omega_k)t} \tilde{b}_k \quad (4.15)$$

by solving them, it can be proven that the probability for the two-level emitter to remain in the excited state is an exponentially decaying function in time:

$$\frac{d\tilde{r}}{dt} = -\gamma(\omega) \tilde{r} \quad (4.16)$$

Where γ is the inverse of the excited state mean lifetime, calculated as:

$$\gamma(\omega) = 2\pi \sum_k |g_k|^2 \delta(\omega_0 - \omega_k) \quad (4.17)$$

Thus, a lifetime limited transition leads to a (*homogeneously* broadened) emission line with Lorentzian shape .

4.2 Decoherence Processes in Single Photon Emission

The further step is to describe the effect of external fluctuating forces acting on the two-level system representing our emitting center. This means that, in the Hamiltonian (4.10), the previously neglected terms accounting for strain, electric and magnetic coupling must be included. When constant, these forces have no dynamical effect on the emission line shape but may result in a shift of the $\hbar\omega_0$ resonance energy between the ground and excited states and a relative shift of the homogeneous line on the frequency domain. On the other side, their fluctuation may instead change the profile of the emitted photon function. To represent this phenomena in the most general terms, a specific potential function must be included in (4.10). From this point, we will use the procedure explained in [38]. As fluctuations are modeled as general stochastic processes, we can define one, discrete in

time, as:

$$\tilde{f}_n = r\tilde{f}_{n-1} + \sigma\sqrt{1-r^2}\tilde{x}_n \quad (4.18)$$

with n being a progressive time index and \tilde{x}_n a set of normally distributed, independent random variables (expressing, in our particular physical picture, the potential value change at a certain time) obeying to:

$$E(\tilde{x}_n) = 0 \quad (4.19a)$$

$$E(\tilde{x}_n, \tilde{x}_m) = \delta_{mn} \quad (4.19b)$$

Given that $E(\tilde{x}_n)$ represents the first order momenta and $(\tilde{x}_n, \tilde{x}_m)$ the second. The parameter r defines instead the time correlation of \tilde{f}_n , so it weightens how much the history of the function (potential) at the $n-1$ instant contributes to the \tilde{f}_n value at the time n . By solving equation (4.18), one can obtain:

$$\tilde{f}_n = \sigma\sqrt{1-r^2} \sum_{m=0}^{\infty} r^m \tilde{x}_{n-m} \quad (4.20)$$

And from this expression, it is easy to switch to a Markov chain continuous in time, characterized by a exponentially decaying second order momentum, by substituting r with a function of the form $r = e^{-\beta dt}$ and setting the time as $t = ndt$:

$$E(\tilde{f}(t)) = 0 \quad (4.21a)$$

$$E(\tilde{f}(t), \tilde{f}(t')) = \sigma^2 e^{-\beta|t-t'|} \quad (4.21b)$$

We have now a mathematical tool for modelizing, in a simple way, a fluctuating force that acts on the Nitrogen-Vacancy center with different time correlation properties that may represent, i.e. a drift or a completely random temporal evolution with gaussian module (also called *white noise*). We will add to the Hamiltonian (4.10) a term accounting for the last one:

$$\hat{H} = \left[\frac{\hbar\omega_0}{2} + \frac{\tilde{f}(t)}{2} \right] \hat{\sigma}_z + \sum_k \hbar\omega_k \left(\hat{a}_k^\dagger \hat{a}_k + \frac{1}{2} \right) + i\hbar \sum_k g_k \left(\hat{\sigma}^+ \hat{a}_k - \hat{\sigma}^- \hat{a}_k^\dagger \right) \quad (4.22)$$

In the two-level system framework previously defined, the possible eigenfunctions of (4.22) may be:

$$\left| \tilde{\psi}(t) \right\rangle = \tilde{r}(t) e^{-i\omega_0 t/2 + i\tilde{g}(t)/2} |0\rangle_f |e\rangle + \sum_k \tilde{b}_k(t) e^{i\omega_0 t/2 - i\omega_k t + i\tilde{g}(t)/2} a_k^\dagger |0\rangle_f |g\rangle \quad (4.23)$$

where $r(t)$ are the time-dependent amplitude coefficients for the excited state and $b_k(t)$ are a set of amplitude coefficients for the ground state coupled to a single photon of frequency ω_k , as defined before. Furthermore, $\tilde{g}(t)$ represents:

$$\tilde{g}(t) = \int_0^t \tilde{f}(t') dt' \quad (4.24)$$

Solving the Schroedinger equation by substituting (4.23) into (4.22) one can obtain the dynamics of the coefficients:

$$\frac{d\tilde{r}}{dt} = -i\tilde{f}(t)\tilde{r} - i \sum_k g_k e^{i(\omega_0 - \omega_k)t} \tilde{b}_k \quad (4.25a)$$

$$\frac{d\tilde{b}_k}{dt} = -ig_k e^{i(\omega_0 - \omega_k)t} \tilde{b}_k \quad (4.25b)$$

integrating the second one, and using the result in the first, we have:

$$\frac{d\tilde{r}}{dt} = -i\tilde{f}(t)\tilde{r} - \int_0^t dt' \sum_k g_k^2 e^{i(\omega_0 - \omega_k)(t-t')} \tilde{r}(t') \quad (4.26)$$

here, the Weisskopf-Wigner approximation[quote] gives:

$$\sum_k g_k^2 e^{i(\omega_0 - \omega_k)(t-t')} \rightarrow \gamma \delta(t - t') \quad (4.27)$$

and the further integration of \tilde{r} over t brings to:

$$\tilde{r}(t) = e^{-\gamma t/2} e^{-i\tilde{g}(t)} \quad (4.28)$$

Finally, using this expression into the equation that gives b_k in time, one has:

$$\tilde{b}_k(\infty) = -ig_k \int_0^\infty dt e^{[-i(\omega_0 - \omega_k) - \gamma/2]t} e^{-i\tilde{g}(t)} \quad (4.29)$$

By switching to a continuum of photon modes the previous expression can be used to derive a photon wavefunction on a frequency space; it is important to notice that this wavefunction has not the same properties of a quantum mechanical one for a massive particle, as it is not a position operator eigenstate. Nevertheless, its explicit form is:

$$\tilde{\alpha}(\omega) = -i\sqrt{\frac{\gamma}{2\pi}} \int_0^\infty dt e^{[-i(\omega - \omega_0) - \gamma/2]t} e^{-i\tilde{g}(t)} \quad (4.30)$$

Knowing that the radiation intensity spectra is $I(\omega) = E(|\tilde{\alpha}(\omega)|^2)$, it is possible to derive this quantity using the (4.30). Considering a generic stationary fluctuating potential acting on the emitter, a change of variables is made to obtain:

$$I(\omega) = \frac{1}{2\pi} \int_{-\infty}^{+\infty} d\tau e^{i(\omega - \omega_0)\tau - \gamma|\tau|/2} E\left(e^{-i \int_0^\tau dt' \tilde{f}(t')}\right) \quad (4.31)$$

And considering the specific random potential described in eq. (4.21), one can obtain the complete frequency-dependent intensity spectra for photons emitted from a two-level system, coupled to a continuum of light modes and with a random Markovian fluctuating potential acting on it:

$$I(\omega) = \frac{1}{2\pi} \int_{-\infty}^{+\infty} d\tau e^{i(\omega - \omega_0)\tau - \gamma|\tau|/2 - \frac{\sigma^2}{\beta} [|\tau| - \frac{1}{\beta} (1 - e^{-\beta|\tau|})]} \quad (4.32)$$

4.3 The Homogeneous Broadening Limit

From the model described in the previous section, it is possible to discuss some limit cases. The first one occurs when the noise fluctuation rate is much higher than the photon emission rate, so when $\beta \gg \gamma$. Such situation leads to the term $1 - e^{-\beta|\tau|}$ being dropped from (4.32). The integral is

therefore:

$$I(\omega) \approx \frac{1}{2\pi} \frac{\gamma + \frac{2\sigma^2}{\beta}}{(\omega - \omega_0)^2 + \frac{1}{2} \left[\left(\gamma + \frac{2\sigma^2}{\beta} \right) \right]^2} \quad (4.33)$$

Thus, the emitting line has a Lorentzian profile in which the $2\sigma^2\beta^{-1}$ term adds to the emission lifetime inverse increasing the distribution width but not the overall shape.

4.4 The Inhomogeneous Broadening Limit

The second limit case happens when the fluctuating potential changes slowly if compared to the excited state lifetime. So, for $\beta \ll \gamma$, the intensity spectra is:

$$I(\omega) \approx \frac{1}{2\pi} \int_{-\infty}^{+\infty} d\tau e^{i(\omega - \omega_0)\tau - \frac{\gamma}{2}|\tau| - \frac{\sigma^2\tau^2}{\beta}} \quad (4.34)$$

This is a Voigt profile, representing the convolution of a Lorentzian with a Gaussian. A simplified physical picture induced by this expression involves an emission line, homogeneously broadened, with lorentzian shape and narrow width, that ‘jumps’ in random directions in the frequency space within a gaussian envelop. The latter accounts for the varying external forces that act on the emitting center with different modules and directions for different excitation-emission cycles, leading to environmental induced energy shifts or degeneracy removals in the center levels. Such process is called also decoherence, while the generated emission line is said to undergo spectral diffusion. Understanding the timescale and the mechanism of this process is necessary to have a probability success estimation for the Hong-Ou-Mandel effect, as it is easy to imagine that only photons emitted within an average τ time will show the same identical intensity spectra (and wave-function).

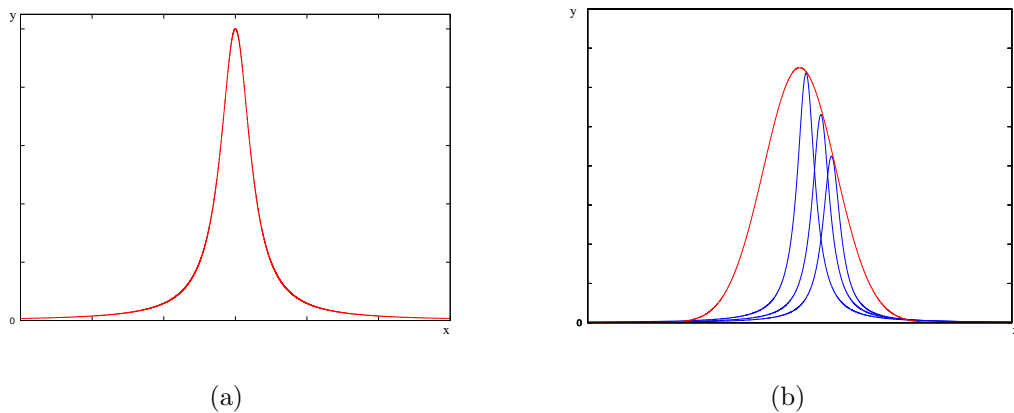


Figure 4.1: Profiles of a generic Lorentzian-shaped emission line (a) and of a Voigt-shaped emission line (b) in which the final signal is the convolution of a gaussian, representing the inhomogeneous broadening process, and a lorentzian, stemming from homogeneous broadening.

Chapter 5

Photon Correlation Interferometry

The problem of spectral diffusion, as addressed in the previous chapter, represents a main obstacle in the development of solid-state single photon sources for QIP applications. Inhomogeneous broadening that stems from the coupling between the emitter and the surrounding environment, is caused in such systems by slow-varying (if compared to the excited state lifetimes) potentials which arise in the material and act on the photon source energy levels. In the Nitrogen-Vacancy center, these effects might involve i.e. strain stresses (which, at low temperature, are static), magnetic couplings and electric Stark shifts; other terms may also be mentioned (as hyperfine couplings) although they are much weaker, as discussed in Chapter 3 and 4. The simplest method to investigate experimentally spectral diffusion would be a direct observation of the emission line time evolution with a spectrometer [59, 61, 63]. However, such approach is often unpracticable, mostly when dealing with single emitters which give weak ZPL signals (due to their intrinsic physical nature or strong first-order phonon coupling) and relatively fast spectral jumps [64] within the gaussian envelope. To overcome these limits, different techniques were introduced in the last years. A method proposed in [61] relies on a Hambury-Brown-Twiss setup with two spectrometer units in front of each APD. Under the assumption that the inhomogeneous line is symmetric and has a fixed central frequency (which is, in case of most quantum emitters, not necessarily true) the two spectrom-

eters are used to filter opposite sides of the broad emission line, allowing photons belonging to different frequency intervals to reach each detection unit. In auto-correlation mode, two spectrometers filter the same side of the line respect to the center, while in cross-correlation mode, intervals from two opposite sides are filtered. By comparing these two measurements, one can estimate the average fluctuation time of the homogeneous line. However, this approach shows its limits when dealing with asymmetric emission lines and it has, in any case, spectrometer-limited resolution. Other techniques have a completely different view on the problem, and implement interferometrical measurements to map the frequency distribution of emitted light into an intensity distribution, and deduce from it the characteristic fluctuation times. Photon Correlation Fourier Spectroscopy [60, 62] was the first step in this direction: it uses a Michelson interferometer, with one moving arm and a mounted dithering mirror, to convert the emission line frequencies into intensity variations, detected by two APD units. However, in the first realizations, the presence of unfixed parts and the setup complexity has brought serious time resolution limits, which allowed the identification of spectral diffusion rates not lower than $100 \mu s$. These problems were successfully solved in a way that the sensitivity went as high as the instrumental limits. In the present work, we use a PCFS derivate setup based on a fixed Mach-Zehnder interferometer with an Hanbury-Brown-Twiss section on the downline. The Mach-Zehnder introduces an arbitrary chosen number of interference fringes within the Gaussian inhomogeneous line, thus giving the frequency to intensity conversion. The HBT setup is used to perform cross-correlation measurements (second order coincidence events from two different interferometer arms) or auto-correlation measurements (second order correlated detection events with no interferometry) with a time resolution down to the photon counting device limits (lower than 100 ps). Furthermore, as the $g^{(2)}(\tau)$ functions are normalized, the setup is stable respect to intensity fluctuations that arise from the opto-mechanical section (i.e. sample drift out of the confocal volume). In the following sections, the setup basical elements are described, as also the experimental information that can be directly obtained from them. Finally, a method used to estimate the spectral diffusion time from these data is presented.

5.1 Mach-Zehnder Interferometer

The Mach-Zehnder interferometer is a standard scheme used in various physical applications. In the polarization-independent configuration, it is made up of a 50/50 beamsplitter which splits the incoming photon along two paths (modes) with different probability amplitudes. Each path (or arm) has a different length, that induces a phase-shift between the two modes. Two reflective mirrors send back the radiation to a second 50/50 beamsplitter, where the photon is recombined. The pictures below give a representation of the functioning.

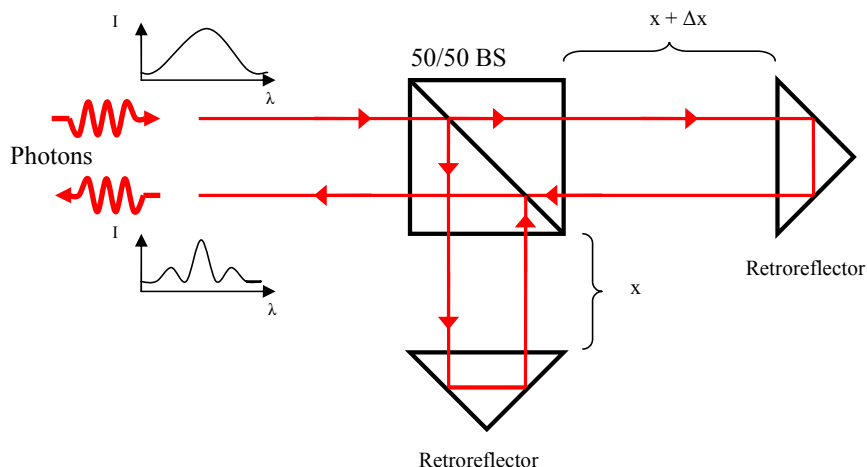


Figure 5.1: Illustration of a folded Mach-Zehnder interferometer. The incident light is splitted by a 50/50 beamsplitter and addressed toward two retroreflectors at distance respectively x and $x+\delta x$. The path difference induces a phase shift between the two light modes, that are recombined on the same BS

In quantum mechanical formalism the input state, a single-mode photon of definite polarization, spans two possible situations, that describe its entering mode in the interferometer:

$$|1\rangle_a \times |0\rangle_b = \begin{pmatrix} 1 \\ 0 \end{pmatrix} \quad |0\rangle_a \times |1\rangle_b = \begin{pmatrix} 0 \\ 1 \end{pmatrix} \quad (5.1a)$$

The first BS performs the transformation:

$$U_{BS} = \frac{1}{\sqrt{2}} \begin{pmatrix} 1 & 1 \\ 1 & -1 \end{pmatrix} \quad (5.2)$$

which, if the input state is $|1\rangle_a \times |0\rangle_b$, gives as output:

$$U_{BS} \begin{pmatrix} 1 \\ 0 \end{pmatrix} = \frac{1}{\sqrt{2}} \begin{pmatrix} 1 & 1 \\ 1 & -1 \end{pmatrix} \begin{pmatrix} 1 \\ 0 \end{pmatrix} = \frac{1}{\sqrt{2}} \begin{pmatrix} 1 \\ 1 \end{pmatrix} \quad (5.3)$$

If we suppose the second path to induce a phase shift of $\phi = 2\pi x/\lambda$ with respect to the first (due to the difference in length x), matrix notation allows this to be written as:

$$U_\phi = \begin{pmatrix} 1 & 0 \\ 0 & e^{i\phi} \end{pmatrix} \quad (5.4)$$

and:

$$U_\phi \frac{1}{\sqrt{2}} \begin{pmatrix} 1 \\ 1 \end{pmatrix} = \frac{1}{\sqrt{2}} \begin{pmatrix} 1 & 0 \\ 0 & e^{i\phi} \end{pmatrix} \begin{pmatrix} 1 \\ 1 \end{pmatrix} = \frac{1}{\sqrt{2}} \begin{pmatrix} 1 \\ e^{i\phi} \end{pmatrix} \quad (5.5)$$

Finally, the two modes are recombined by the second beamsplitter, allowing so the photon to interfere with itself (via mixing the probability amplitudes for each arm):

$$\frac{1}{2} \begin{pmatrix} 1 + e^{i\phi} \\ 1 - e^{i\phi} \end{pmatrix} = \frac{1}{2} \begin{pmatrix} 1 & 1 \\ 1 & -1 \end{pmatrix} \begin{pmatrix} 1 \\ e^{i\phi} \end{pmatrix} \quad (5.6)$$

Where an overall phase term is neglected. Hence, the probability of the photon to be found at the output L or R is deduced as:

$$P_L = \left| \frac{1}{2} (1 + e^{i\phi}) \right|^2 = 1 + \cos \phi \quad (5.7a)$$

$$P_R = \left| \frac{1}{2} (1 - e^{i\phi}) \right|^2 = 1 - \cos \phi \quad (5.7b)$$

This quantity is proportional to the EM intensity at the second beamsplitter exits. It must be pointed out that in real interferometers, a perfect interference is never achieved, due to non-ideal properties of the fundamental components (as beamsplitters or retro-reflectors, that have non-zero losses),

beam disturbances and non-perfect overlaps. Thus, a unitary contrast is never achieved, but its value c depends on the experimental conditions and setup, and is calculated as:

$$c = \frac{I_{max}^\lambda - I_{min}^\lambda}{I_{max}^\lambda + I_{min}^\lambda} \quad (5.8)$$

where λ is the radiation wavelength. Hence, a single-photon interferometric intensity modulation function is defined as:

$$m_{L/R} = 1 \pm c \cos \phi \quad (5.9)$$

5.2 Photon Correlation Interferometry Setup

Correlation measurements on self-interfered photons can be performed by coupling the Mach-Zehnder outputs with two avalanche photo-diodes, connected to a time-correlated photon counting module. The available information obtained from each detection is the photon intensity $\hat{I}_{L/R}(t)$ at the left or right interferometer outputs:

$$\hat{I}_{L/R}(t) = \eta_{L/R} m_{L/R}(t) \hat{N}(t) \quad (5.10)$$

Where $\eta_{L/R}$ accounts for the overall APD quantum efficiency, $\hat{N}(t)$ is the photon number operator as defined in chapter 2 and $m_{L/R}(t)$ is the modulation function introduced in (5.9). With the configuration previously described, different sorts of correlation measurements can be performed. The second order autocorrelation function is obtained by simply closing one arm of the interferometer (or, in the case of NV centers, using the whole fluorescence spectrum). Its expression is the same used in chapter 2.2:

$$g^2(\tau) = \frac{\langle : \hat{I}(t) \hat{I}(t+\tau) : \rangle_t}{\langle \hat{I}(t) \rangle_t \langle \hat{I}(t+\tau) \rangle_t} \quad (5.11)$$

With $\hat{I}(t)$ being the non-modulated intensity operator and $::$ denoting normal ordering.

$$\hat{I}(t) = \eta \hat{N}(t) \quad (5.12)$$

Nevertheless, the second order cross-correlation function of the two interferometric paths is calculated as:

$$g_{L/R}^2(\tau) = \frac{\langle \hat{I}_L(t) \hat{I}_R(t+\tau) \rangle_t}{\langle \hat{I}_L(t) \rangle_t \langle \hat{I}_R(t+\tau) \rangle_t} \quad (5.13)$$

By substituting (5.10) into the previous expression, it is possible to see that:

$$g_{L/R}^2(\tau) = g^2(\tau) \langle m_L(t) m_R(t+\tau) \rangle_t \quad (5.14)$$

What is therefore required, is a method that relates the quantities in (5.14) with certain characteristics of the inhomogeneous process that can be used to gain further knowledge about the physical properties of the emitter.

5.3 Spectral Diffusion Characteristic Time

The auto-correlation function and the interferometric modulated cross-correlation function of a single-photon source can be used to calculate an average spectral diffusion time, defined as the mean time interval between two jumps of the homogeneous emission line within the broad inhomogeneous envelope. Here, the main assumption (introduced in chapter 4 model) is that the homogeneous line fluctuations are caused by a potential which evolution is represented by a stochastic process (random walk), stationary in time and with exponentially decreasing correlation between its points. Defining $\lambda(t)$ as the emitted photon frequency, it is useful to remind the interferometric modulation:

$$m_{L/R}(t) = 1 \pm c \cos\left(\frac{2\pi x}{\lambda(t)}\right) \quad (5.15)$$

The dependence on the emission wave-length at a certain time can be easily noticed. Hence, computing the cross-correlation function can be done by evaluating the term $\langle m_L(t) m_R(t+\tau) \rangle_t$. By introducing a characteristic

function $\chi(t, \tau)$ for the spectral jump event in the interval $[t, t + \tau]$:

$$\chi(t, \tau) = \begin{cases} 1 & \text{if a jump doesn't occur} \\ 0 & \text{if a jump occurs} \end{cases} \rightarrow \lambda(t) = \lambda(t + \tau) \quad \rightarrow \lambda(t) \neq \lambda(t + \tau) = \lambda(t') \quad (5.16)$$

It is possible to separate the second term in (5.14) as follows:

$$\langle m_L(t) m_R(t + \tau) \rangle_t = \langle \chi(t, \tau) m_L(t) m_R(t + \tau) \rangle_t + \quad (5.17a)$$

$$+ \langle (1 - \chi(t, \tau)) m_L(t) m_R(t + \tau) \rangle_t \quad (5.17b)$$

where the first part of (5.17) accounts for the unchanged spectral position and the second for a shift of the homogeneous line wavelength in a certain time τ . The characteristic functions can be brought out of the time-average: when separately integrated in t , they give a probabilistic information about the event represented by their associated value:

$$p(\tau) = \langle \chi(t, \tau) \rangle_t \quad (5.18a)$$

$$1 - p(\tau) = \langle 1 - \chi(t, \tau) \rangle_t \quad (5.18b)$$

Considering the wavelength expressions defined in (5.16), equation (5.17) can be rewritten as:

$$\langle m_L(t) m_R(t + \tau) \rangle_t = p(\tau) \langle m_L(t) m_R(t) \rangle_t + (1 - p(\tau)) \langle m_L(t) m_R(t') \rangle_{t,t'} \quad (5.19)$$

The two integrals arising from the interferometric modulation terms in (5.17) may now be calculated. In the case of a jump event, $\lambda(t)$ and $\lambda(t')$ are uncorrelated; that means that the integration can be performed both in t and t' . By assuming several interference fringes within the gaussian envelope, we can substitute the cosine arguments respectively with $\frac{2\pi x}{\lambda(t')} \rightarrow \phi'$

and $\frac{2\pi x}{\lambda(t)} \rightarrow \phi$ and integrate in the range $0 \rightarrow 2\pi$. This yields:

$$\langle m_L(t) m_R(t') \rangle_t = \int m_L(t) m_R(t') dt = \quad (5.20a)$$

$$= \int \left(1 + c \cos\left(\frac{2\pi x}{\lambda(t)}\right)\right) \left(1 - c \cos\left(\frac{2\pi x}{\lambda(t')}\right)\right) dt = \quad (5.20b)$$

$$= \int_0^{2\pi} d\phi' \int_0^{2\pi} d\phi (1 + c \cos \phi) (1 - c \cos \phi') = 1 \quad (5.20c)$$

w where the result has been normalized. With the same technique, we can solve the case of having no jump events

$$\langle m_L(t) m_R(t) \rangle_t = \int m_L(t) m_R(t) dt = \quad (5.21a)$$

$$= \int \left(1 - c^2 \cos^2\left(\frac{2\pi x}{\lambda(t)}\right)\right) dt = \quad (5.21b)$$

$$= \int_0^{2\pi} d\phi (1 - c^2 \cos^2 \phi) = 1 - \frac{c^2}{2} \quad (5.21c)$$

Substituting the results into (5.14) leads to:

$$g_{L/R}^2(\tau) = g^2(\tau) \langle m_L(t) m_R(t + \tau) \rangle_t = \quad (5.22a)$$

$$= g^2(\tau) \left[1 - \frac{c^2}{2} p(\tau)\right] \quad (5.22b)$$

We may now write an expression that relates the probability of having no spectral jumps (within the time τ) with the cross-correlation and autocorrelation functions that may be acquired experimentally:

$$p(\tau) = \frac{2}{c^2} \left[1 - \frac{g_{L/R}^2(\tau)}{g^2(\tau)}\right] \quad (5.23)$$

For an uncorrelated process, it can be assumed (based on the rate equation model in [61]) the transition probability from one point to another to have the form of an exponential decaying function. Therefore, it can be expressed

as:

$$p(\tau) = \exp\left(-\frac{\tau}{\tau_c}\right) \quad (5.24)$$

where τ_c is the characteristic jumping time; the rate is obtained from its inverse. Hence a setup that combines interferometry with correlation measurements gives us all the information required to estimate the timescale of spectral diffusion down to the picosecond scale, under the only assumption that the fluctuating forces acting the physical emitter are stationary and time-uncorrelated.

Chapter 6

The Experimental Setup

The procedure used to study ZPL inhomogeneous broadening phenomena in single nanodiamond-based Nitrogen-Vacancy centers is grounded on the emitter description made in chapter 3 and chapter 4, and interferometry-correlation spectroscopy presented in chapter 5. The complete setup that has been used is described in the sections below. Before switching to a detailed overview of the configuration we adopted, with the corresponding devices, the sample preparation routine and the sample characteristics are presented.

6.1 Solid Immersion Lenses

Solid Immersion Lenses have been used both as nanodiamond supports and mainly as optical devices for increasing the fluorescence light collection efficiency and reducing the excitation spot size [66]. Namely, a SIL is an object made of a material with high refraction index [65] (in our case Zirconium Dioxide, $n = 2.17$ at 600nm) that increases the effective numerical aperture (NA_e) of the microscope, calculated as:

$$NA_e = n \cdot \sin\alpha \quad (6.1)$$

where n is the refractive index of the medium in which the objective is focusing, and α its maximum angle of acceptance. Hence, the operative principle is the same as oil immersion microscopy. Moreover, the reduction

of the incident beam effective wavelength that stems from the increased n index in the focusing material brings to a higher resolving power, defined according to the Rayleigh criteria:

$$\delta = 0,61 \frac{\lambda}{NA_e} = 0,61 \frac{\lambda}{nNA_a} \quad (6.2)$$

in which δ is the minimal separation required between two point objects in order to make them optically distinguishable and NA_a the objective in-air numerical aperture. A scheme is helpful to visualize these features: A fundamental aspect is here represented by the SIL geometry, that affects

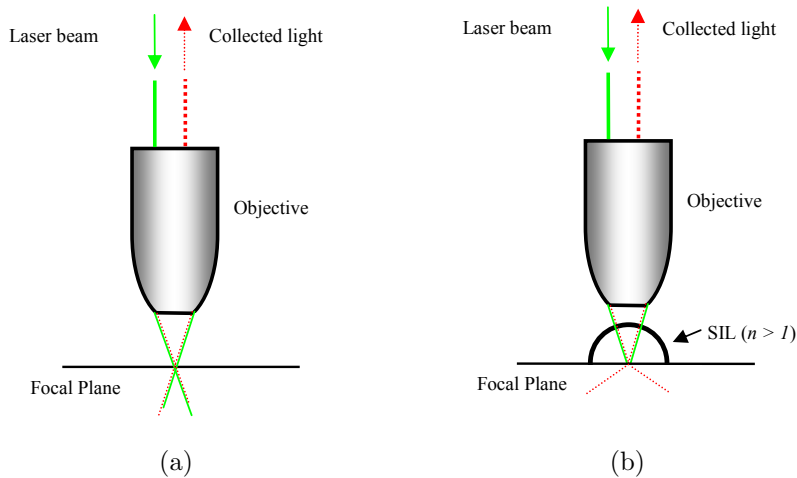


Figure 6.1: Illustration of an hemispherical SIL [67] positioning and functionality: by focusing in a media with higher refraction index (b), the effective microscope (a) numerical aperture is enhanced. The specimen, in this case, has to be placed on the SIL flat top.

directly its functionality. Here, two main designs are available. For a standard hemispherical solid immersion lens [67] one expects, in ideal conditions, no refraction at the passage air-to-SIL because the incident rays enter the hemispherical region perpendicularly to the surface. Furthermore, no chromatic aberration is observed. In a Weierstrass scheme, the SIL consists in a truncated sphere [68, 69, 70] of height $(1 + 1/n)r$, with r being its radius. Such geometry imposes to consider even for ideal conditions the effects of chromatic aberration, suggesting therefore to work with monochromatic light, but on the other side enhances the effective numerical aperture by a n^2 factor. In Fig. 6.2, these two models are represented:

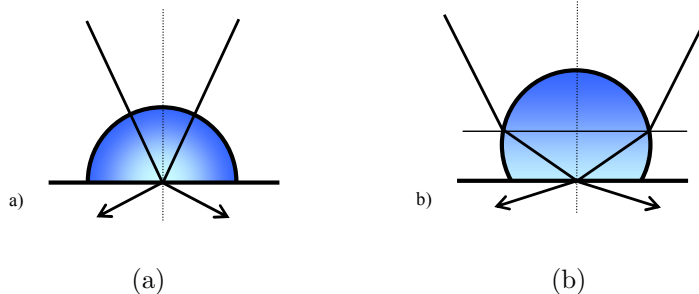


Figure 6.2: Hemispherical (a) and Weierstrass SIL geometries are depicted. In both of the cases, the sample has to be placed on the flat side. The Weierstrass configuration improves dramatically the numerical aperture, but suffers much aberrations.

For both schemes, the specimen are either deposited on the flat SIL surfaces or collocated at a close distance to them. This implies another phenomena to be taken into account, that is the emission-dipole pattern modification for a source located in proximity of a material with different refraction index. In such conditions, the dielectric acts like a near-field antenna, enhancing the emission toward itself; this behaviour has been investigated with FDTD (Finite Difference Time Domain) simulations, in which the emitting center was represented by a single dipole, oscillating at a 10 nm distance from the interface, with different orientations respect to it. For the parallel orientation and a SIL with $n = 2,15$, it has been calculated that 86,2 % of the photons are emitted toward the dielectric (and therefore, the objective) and only 13,7 % in the air [71]. Due to their tolerance and low aberrations even in non-ideal conditions, hemispherical SILs of 1 mm radius were chosen for our experiments. The combination of these previously described features (lower focus size, enhanced emission toward the objective, higher numerical aperture) brings for such devices to an improved collection efficiency by a factor in the range from 7.6 to 15.2 times respect to conventional supports in air[71]. Before each deposition, every Solid immersion lens had to undergo a cleaning procedure, that consisted in a 30 minutes treatment with deionized water, a following 30 minutes treatment with a 2% solution of *Hellmanex II* (*Hellma*) cleaner and a last 30 minutes water cleaning. All of these steps were carried out in a ultrasonic bath. Finally the SILs were washed with Methanol and ultimatively with Isopropanol. The nanodiamond deposition was performed immediately after the cleaning procedure.

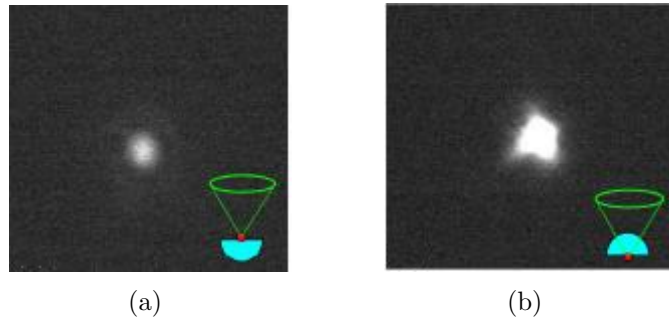


Figure 6.3: Fluorescent emitters (beads) are used to estimate the collection efficiency increase due to the SILs. The CCD camera images show an appreciable enhancement of the signal in (b), where the focusing happens into the SIL, if compared with (a), where the focusing occurs in air. Image distortions in (b) are caused by SIL-induced aberrations

6.2 Sample Description and Preparation

Nitrogen-Vacancy rich nanodiamonds are commonly available for standard research applications. In the measurements, we used high-quality Type Ib nanodiamonds obtained via milling. The diameter of these particles was in the range 30-150 nm, although the most interesting size interval for having single (and not multiple) NV centers in each nanodiamond goes from 40nm to 70nm[72]. The presence of two or more color defects imply the simultaneous excitation/fluorescence for all of them, easily detectable via an auto-correlation measurement. Namely, the latter would show a $g^{(2)}(0)$ function equal or higher than 0.5, pointing clearly to a many-photon regime.

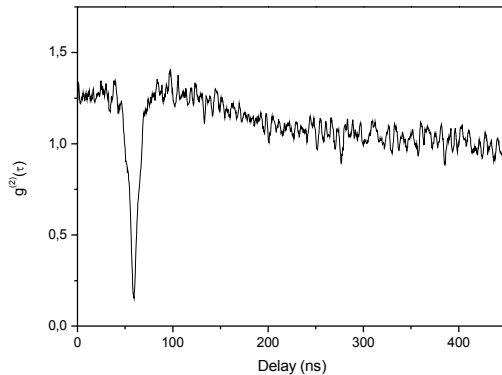


Figure 6.4: Experimentally determined $g^{(2)}(\tau)$ autocorrelation functions via Hanbury-Brown-Twiss scheme. The dip (called *antibunching dip*) going below 0.2 indicates clearly a subpoissonian regime and a single photon emission in Fock states. This doesn't happen at zero delay (as expected) for cable and electronic-induced delays. Autocorrelation functions having dips above 0.2 but under 1.0 point yet a sub-poissonian statistics but not on Fock states; in this case, the reason is having two or more single photon sources (NV) within the focal volume

In our case, nanodiamonds (NDIA) were available in water suspension (0,1 mg/mL of NDIA). Two different techniques were used to deposit a layer on appropriate substrates (Solid Immersion Lenses, described in the following section). The pre-treatment consisted in a 30 minutes ultrasonic bath, required to revert the clustering process between nanodiamonds that might occur in a stable water solution. Nevertheless, two possible operative methods were used:

- A quantity of $10 \mu\text{l}$ of NDIA suspension was diluted 1:10 in deionized water and subsequently mixed in the ultrasonic bath for 30min; the following deposition on a SIL top was made by evaporation of 2-3 droplets (approx $1 \mu\text{l}$ each) within 30 minutes time windows.
- $10 \mu\text{l}$ of NDIA were diluted with 1:5 proportion in a 0,02% water solution of Polyvinyl-Alcohol (PVA). The deposition occurs via two single-droplet spin coating passages, each one being 2 minutes long. The optimal spin-coater rotation regime was 2000 rpm.

While the first approach guarantees the highest nanodiamond surface density, it shows also an increased agglomeration of nanoparticles, with the consequent difficulties in having single ones within the confocal volume. On the

other side, the second method uses a polymer (with relatively high sticking coefficient to Zirconium Dioxide) that ‘traps’ nanodiamonds on the flat SIL surface, although in a low-density layer (without PVA, the spin-coating generally results in a nanoparticle dispersion on the lens borders). Therefore, the latter method has been usually adopted and the sufficient nanodiamond density tested with a fast room-temperature fluorescence scan.

6.3 General Setup Scheme

The setup used to implement the interferometry-correlation method is made of a certain number of functional elements. These are shown in the underlying scheme. The corresponding details are described in the sections below.

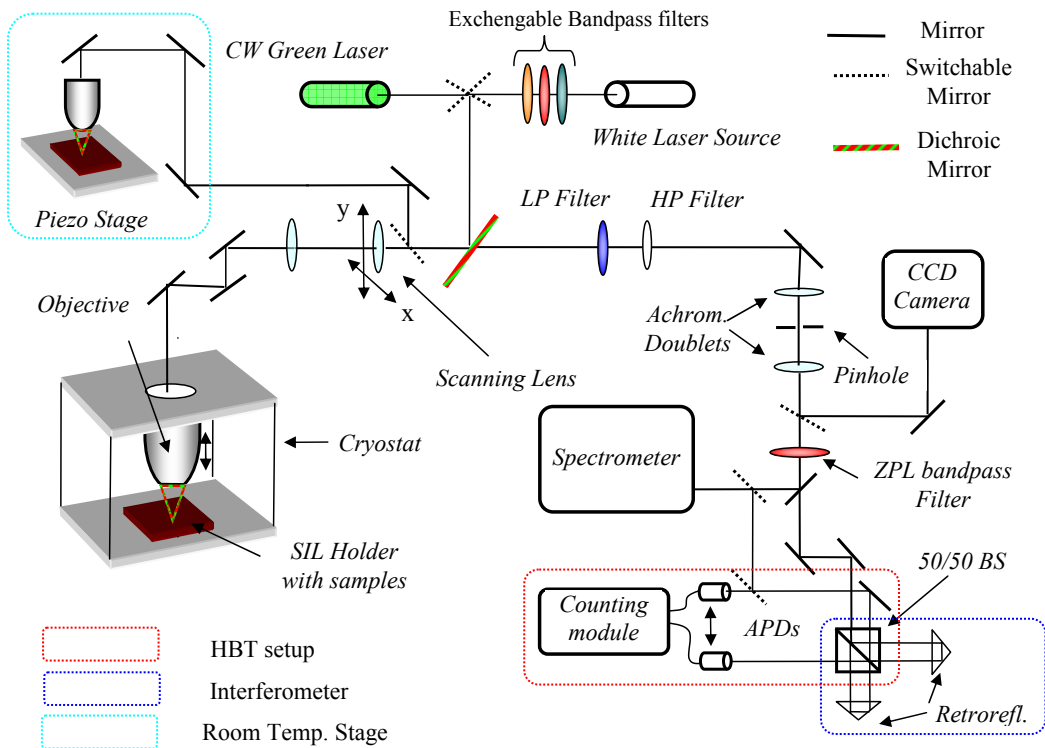


Figure 6.5: General scheme of the used setup. The dashed, coloured lines point out different functional elements that are used to perform specific operations. Mirrors and switchable mirrors are indicated as solid and dashed black segments. Short Pass and Long Pass filters are represented SP and LP

6.4 Cryostat

The single nanodiamond-coated SILs were positioned in a *Cryovac Micro-Cryo* cryostat, with continuus flow liquid-helium cooling circuite (down to 5K) that lowers the specimen temperature via contact between the helium pipes and the SIL holder. Of particular importance was the fact that the

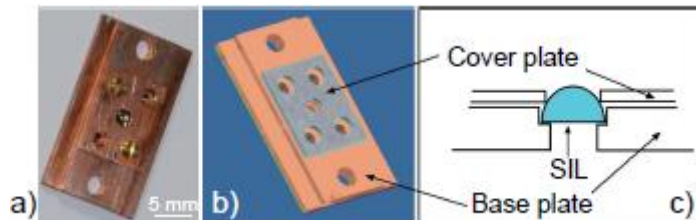


Figure 6.6: Representation of the SIL metallic holder (a) and its technical sketch (b). The SIL position is showed in (c); nanodiamonds are deposited on the flat side, while the pumping laser beam hits firstly the curved surface [71].

objective module could be positioned inside the cryo vacuum chamber. This choice shows the advantage that no interface media lays between the SIL surface and the objective, thus allowing either the use of high NA objectives and the avoiding of beam distortion (due to refraction). Attached to the chamber, a compact *Pfeiffer Vacuum* pump unit provided the ultra-high-vacuum conditions needed for the experiments, either to enable the low-temperature regime or to remove eventual fluoresceing impurities. The unit consisted of a rotative pump coupled turbo-molecular pump, with an ionization gauge device monitoring the pressure. The temperature was kept under control with a separate thermostat and the overall thermal stability has been archieved on $\pm 0,1$ K scales. Furthermore, an integrated circuit was used to warm the SIL support by following a temperature ramp, as needed for checking the temperature-dependency of inhomogeneous broadening processes. To control the rough specimen position respect to the objective, three translation stages were capable of translating one whole cryostat section on the plane perpendicular to the optical module (which was situated in another fixed section) and parallely toward it.

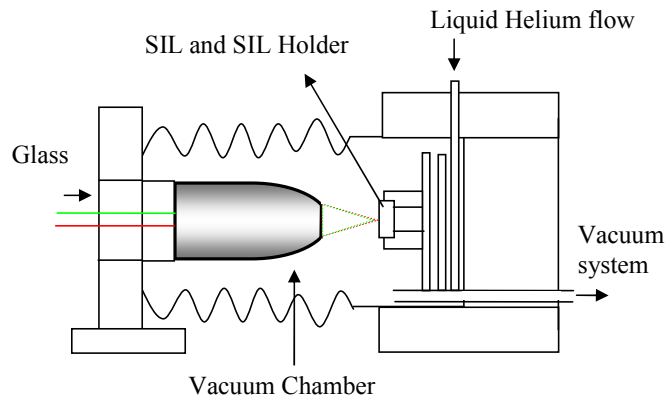


Figure 6.7: Design of the cryostat vacuum chamber with its two sections, hosting the objective (L) and the cooling circuits plus the sample (R)

6.5 Excitation Line

We used two different type of Laser sources to drive the NV center optical transitions:

- A 532nm coherent continuous-wave frequency doubled Laser *china model 200 mW* from *Shanghai Laser and Optics Century*, has been standardly used to induce non-resonant optical transitions between the ${}^3A_2 \rightarrow {}^3E$) energy levels of Nitrogen-Vacancy center. The available power is more than sufficient to reach saturation.
- A continuus white Laser source *NKT photonic SuperK* model, generating the whole spectra of wavelengths between 400nm and 2400 nm with total power of 2 W. The emitted radiation is pulsed with periodicity of 40 or 78 Mhz. To select specific frequencies and perform NV excitations in different intervals of the phonon side bands, a set of 10 nm narrow *Thorlabs* bandpass filters were available. The usable wavelengths were (510, 520, 540, 550, 560, 570, 580, 590, 600)nm.

The EM sources were positioned within the setup in a way that they could accede the optical section with minimal adjustments.

6.6 Optical Section

A confocal scheme was used both to focus the excitation light on the sample and to collect the fluorescence from the NV radiative transitions. This was done by means of a 0.9 NA objective lens *Mitutoyo 100X Plan Apo HR Infinity-Corrected* with large working distance (1.2 mm), collocated in the cryostat. The incident and outgoing beams were separated by a dichroic

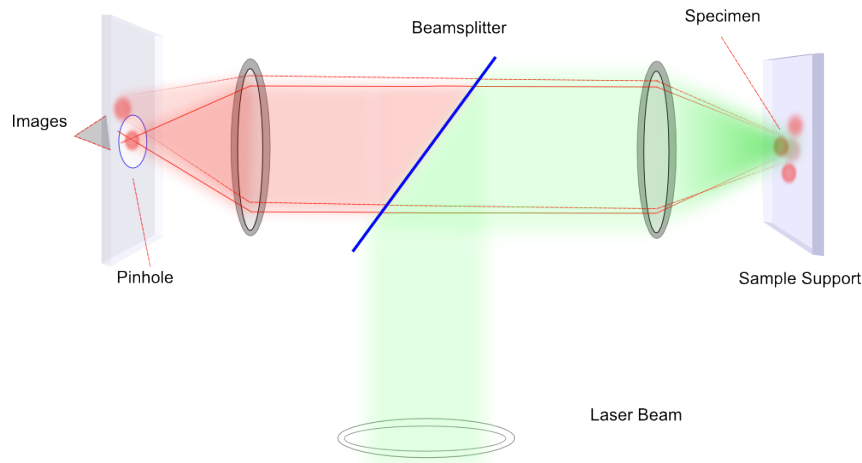


Figure 6.8: The confocal design is used to lower the signal-to-noise ratio during measurements; the principle is to focus via objective lenses the excitation beam and the emitter in the same volume; a beamsplitter separates the two signals sending the sample fluorescence toward a pinhole that allows only a part of the light to pass. In this way, background noises that not arising from the focal volume in which the specific photon source lies are suppressed.

mirror *Thorlabs DMLP567* positioned so that the 90% of the NV-generated photons could reach the detection part with a 10% \div 90% of the pumping radiation arriving to the sample (as that optical line is highly powered, even large losses are well tolerated). Subsequently a short-pass 700 nm filter was used to remove eventual low-energy photons arising from the sample (background emission or impurities) while a long-pass 620nm device filtered out the backscattered excitation Laser light. In a successive section, the emission beam was focused on a 50 μm pinhole (and afterwards expanded) by a couple of 160 mm achromats (magnification of about 80x) as to expect in a confocal setup. Finally, a switchable 7 nm narrow bandpass filter, centered at 640 nm, was installed to select the ZPL light and suppress the phonon side bands. A linear polarization filter was used to achieve the

maximum contrast at the interferometer (orthogonally polarized components cannot interfere in a Mach-Zehnder). The overall scheme was initially aligned with the 532 nm SIL backreflected radiation, and then adjusted on a Nitrogen-Vacancy $^3E \rightarrow ^3A_2$ signal, where the chromatic aberrations could be compensated. As both sample and objective are fixed in the cryostat, the SIL surface scan was performed via a software-controlled motorized lens, capable of spanning the sample support surface on limited but sufficient ranges ($20 \times 20 \mu\text{m}$). For rough adjustments, micrometric screws were used to move the SIL-hosting cryostat section. The vertical axis was controlled via a piezo that moved the objective (and therefore the confocal volume) perpendicularly to the sample.

6.7 Camera

A *Hamamatsu ORCA II* camera was available to perform direct inspections of the focused beam shape and the overall optical section alignment, while it was also useful to visualize directly the NV emitters. Its CCD chip, cooled down to 253K with a Peltier thermocouple, had a 1344 x 1024 resolution and a quantum efficiency of circa 60% at 650nm.

6.8 Mach-Zehnder Interferometer

The interferometer that has been used consisted in a 50/50 beamsplitter cube (performing the functions of both the first and second beamsplitters in a folded Mach-Zehnder scheme as from chapter 5) and two arms ending each one in a retro-reflector. The armlength difference was set up via a micrometric screw mounted on one of the retro-reflectors. Both the contrast adjustment and the fringes per nanometer tuning were performed through the spectrometer, with the procedure described in the following chapter.

6.9 APD Detectors and Counting Module

Every interferometric optical output line was connected to a single photon APD unit *Countmodule from Laser Components*. The two modules we

used, specifically realized for experimental purposes, had a dark count rate ≈ 20 cts/s and a quantum efficiency of c.a. 70% at ZPL frequency. The informations about the photon stream were obtained via an APD-linked time-correlated single-photon counting module, which recorded an arriving time for the photons detected by each photodiode device. This unit, specifically a *PicoQuant Picoharp300*, can measure up to 10 millions cts/s (much higher than the APD tolerance) with a temporal resolution of 4 ps. With short pulsed Ti:Sapphire Lasers, The Instrument Response Function (representing the total timing precision) can go down to 30ps.

6.10 Spectrograph

In order to check the Nitrogen-Vacancy emission spectra or the interferometer functionality, a 500 mm spectrograph unit (Acton SpectraPro 500i) was positioned along one interferometer output. The APD/Spectrograph selection was carried out through a switchable mirror. The unit had a liquid-nitrogen cooled CCD chip and Czerny-Turner design; triple-grating automatically controlled turret, equipped with 600, 1200 and 1800 lines/inch grids provided different resolutions within a characteristic spectral intervals. The maximal achievable resolution is 0,05 nm at 435 nm, while the mechanical scan range lays between 0 nm and 1400 nm; the operative spectral range goes from 185 nm to the far infrared region, depending on the adopted grating. A manually regulated slit is positioned at the spectrograph entrance and used to suppress the background radiation while performing measurements.

6.11 Device Interface and Automatization

The overall process of measurement and data acquisition was software-managed via a Labview program, used to control the scanning mirror motors (through signals given on RS232 ports) and associate to each SIL surface point the APD photon counts as recorded from the PicoQuant module. Correlation measurements were handled by separate softwares and the calculations of interest performed through them. When possible, the mirrors

used to send the light beams to different setup sections were also automated and software controlled, in order to minimize the operator activity on the setup and therefore neglect the induced vibrations or instabilities, as also speed up the experimental procedures. For a fast SIL surface check, an additional stage was available. On this, quick fluorescence scans could be performed through a microscopy unit *NA 0.9 Nikkon* with computer controlled piezo scanners, although only at room temperature and pressure.

Chapter 7

Measuring Spectral Diffusion

The following sections present the experimental realization of photon correlation interferometry for determining the average frequency jump time of the homogeneous emission line within the gaussian inhomogeneous envelope. Different sort of measurements have been performed either to check the model on a multitude of NV centers or to study the dependency of spectral diffusion processes from power excitation, temperature and pumping beam frequency. The particular behaviour is discussed within each section, while a complete data interpretation is given in a following chapter.

7.1 Sample Preparation and Check

A sample check was performed after the deposition of NDIA on a SIL top (chapter 6.2), in order to confirm the presence of single optically distinguishable NV centers on a useful area (the SIL central region, that assures the higher focus quality). This control was done by means of a piezo-driven stage (spanning two axes), on which the sample was mounted, and a *Nikon* (NA 0.9) objective collocated on a further piezoelectric motor (representing thus the third axis) as in Fig. 7.1: The whole procedure was done at standard conditions, so at (296) K temperature and standard pressure, with the green 532 nm CW source. The Laser power was checked with a pyroelectric sensor. After positioning all the optical elements and the specimen, the rough beam adjustment was carried out with SIL backreflected light (lowpass filter removed) and the camera. On the latter, focus quality was

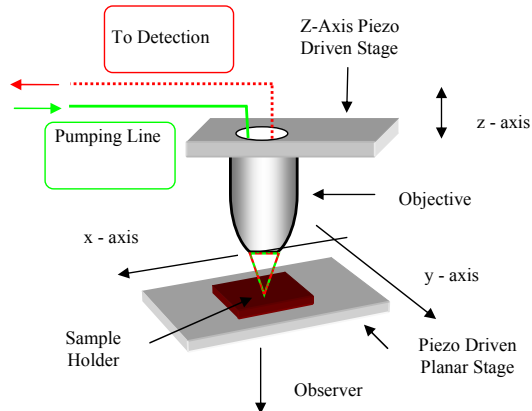


Figure 7.1: A piezoelectric driven stage has been used to perform fast SIL and specimen scans at room temperature. In this way the concentration of stable, non-blinking NV centers in nanodiamonds lying on the SIL central area was quickly determined, as the piezoelectric motors were able to scan wide areas in short time, if compared with the motor-driven lens.

visually monitored until the maximum symmetry and power to surface ratio was achieved (using the piezo and a micrometric screw for the Z-axis and only micrometric screws for the X and Y axes). The beam running to the interferometer was properly aligned with a beam walking procedure, that means using couples of reflective mirror to give respectively a displacement and angle to it. The optimal spot superposition at the interferometer outputs (where the beam is recombined, after being split in the interferometer) was visually checked and adjusted with two micrometric screws mounted on a retro-reflector. The position of the outcoming rays on the APD chips was observed and adjusted through the whole process. Nevertheless, the ultimative fine regulation was done with a very attenuated excitation beam and the activated APDs, by finding the absolute maximum in the counting rate respect to the optical elements fine position. Furthermore, a switchable mirror was been used to link an inteferometer output line to the spectrometer (with the consequent spot adjustment on the internal CCD chip); the Mach-Zehnder fringe amplitude has not been set in this phase but successively. After ultimating these procedures, the lowpass filter was brought back into position (to detect only the NV fluorescence) and the specimen was scanned along the X and Y axes, in order to obtain a map of NV emission intensity over the surface, as in Fig. 7.2:

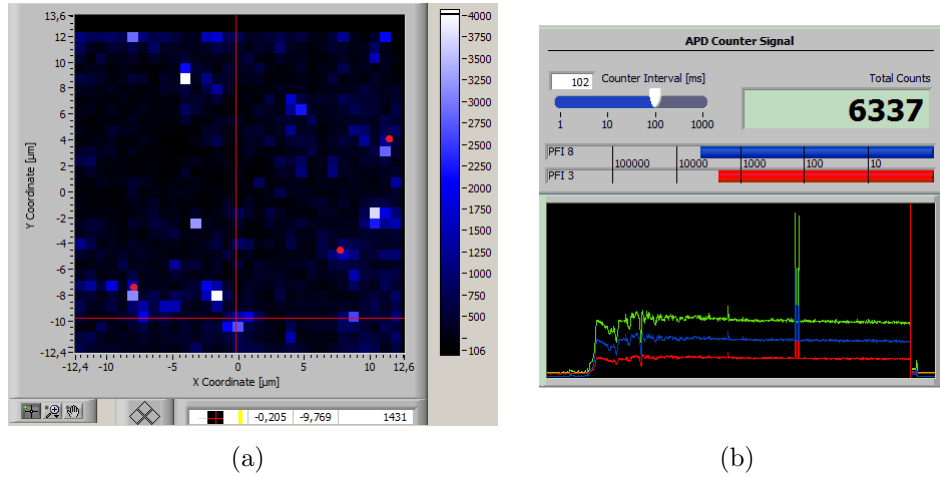


Figure 7.2: Screenshot of some details in the acquisition software. In (a) a map of the SIL central part (Fluorescence intensity Vs. position on the SIL surface) is shown, while in (b) the APD signal (integration time of 102 ms) is recorded, for the spot signed by the cross in (a)

An initial scan usually presented few spots of low intensity, because the setup was optimized for the backreflected green light. Therefore, one of the spots was selected as reference and the beamlines were checked again with the camera and the APDs. Having completed the optimization, the sample was scanned again; a useful NV center was identified by a fluorescence spot on which the autocorrelation function goes, for zero delay, below 0.5, as depicted in Fig. 7.3:

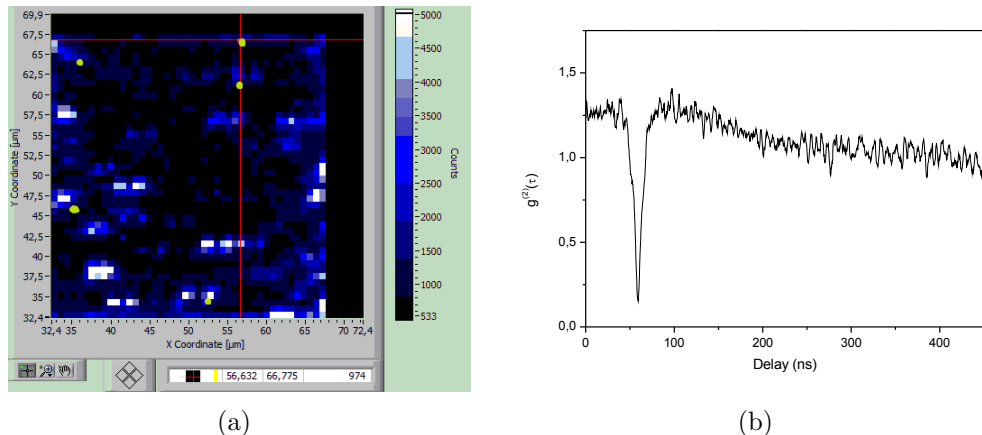


Figure 7.3: Position on the SIL surface, with the focal volume centered on a single NV center (a); autocorrelation function acquired for the same center with an integration time of 10 minutes.

Taking a fluorescence spectra in this situation gives profiles as in Fig. 3.6 where, due to the high temperature, the ZPL is almost completely covered by the phonon side bands, although this is not of interest while performing NV density checks on the SIL surface. By using an under-saturation power (generally $30 \mu W$ to $60 \mu W$), the bright spots on the SIL were checked one by one. A sufficient distinguishable emitters surface density classified the specimen as fit for the spectral diffusion rate measurements at low temperature.

7.2 Cryostat Setup

Spectral diffusion measurements were performed, as explained in chapter 6, in a liquid-helium cooled Cryostat. The proper nanodiamond coated SIL was mounted on a holder and inserted into the vacuum chamber, as shown in the previous chapter. After sealing the device, the attached compact pumping unit was activated and set up to reach the pressure of 10^{-7} mbar. To support degasing, the in-built thermocouple could be used to raise the sample temperature till 323 K and decrease it again. When a stable low pressure was achieved, the external liquid Helium can was connected and a sustained flow induced. By reaching the goal temperature (between 4.6 K and 5.0 K) the flow was gradually reduced until the complete thermal stabilization. To be noticed that the Helium flow to the cryostat was responsible for most of the setup instabilities and vibrations, either for its non-regularity or the physical contact between the cryo chamber and the Helium connector, with the latter being not mechanically isolated from vibrations.

7.3 Single Spectral Diffusion Measurement Procedure

The first part of the proper measurements consisted, as in section 7.2, in the adjustment of the beamlines going to the interferometer, done via camera, spectrometer camera and APDs. Also here, the 532 nm CW pumping line has been used; the power was kept under saturation, in the range

($10 \div 40$) μm on a focusing area smaller than $1 \mu\text{m}^2$. As the optical line going to the cryo was different from the one going to the in-air microscope, the settings had to be reoptimized first for the backreflected green light, and then with the NV fluorescence signal. A further $50 \mu\text{m}$ pinhole was inserted between the achromatic doublets according to a confocal scheme, in order to reduce the noise to signal ratio. With the fully operative setup, a SIL surface scan, sized from $(10 \times 10) \mu\text{m}$ to $(20 \times 20) \mu\text{m}$, was done by means of a motorized lens that displaced equally both the excitation and reflection beams, making thus the Mitsutoyo in-built objective focusing on different SIL coated-side portions. Hence, a map as in Fig. 7.2 and Fig. 7.3 was obtained. Among the observable spots, few with a $g^2(0) < 0.2$ were marked and their spectrum taken, respectively with and without the 7 nm bandpass filter (that allows only the ZPL signal to pass), to check the emission band and background quality. All of these passages were done with one interferometer arm closed. Whence a reliable, stable single NV center was found, with the $g^2(\tau)$ function indicating clearly the emission of light in Fock states (see chapter 2), the Mach-Zehnder was set up by using a micrometric screw under one retro-reflector to change the pathlength difference, in order to get 4-6 fringes within the inhomogeneous broadened ZPL line (around 1 nm of width). Such range is considered optimal when assuming the homogeneously broadened ${}^3E \rightarrow {}^3A_2$ emission line to ‘jump’ in frequency on a scale of 100 GHz within the gaussian envelope and the line itself being around 1 to 10 GHz broad. With a broader line, the frequency to intensity modulation would be effective only with less interference fringes; otherwise each photon would undergo self-interference and the intensity average out. On the other side, the Mach-Zehnder contrast has been optimized too by aligning the beams at the interferometer output. This procedure was followed with the spectrometer by acquiring consecutive spectra, as in Fig 7.4. It has been explained in chapter 5 that measuring the average jump time for spectral diffusion implies measuring autocorrelation and cross-correlation functions of NV emitted light. Thus, once the appropriate single and distinguishable center has been found and focused under the 532 CW, the Laser power was regulated and the 7 nm bandpass filter was kept extracted, so that light was collected in the whole fluorescence spectra. Subsequently, sec-

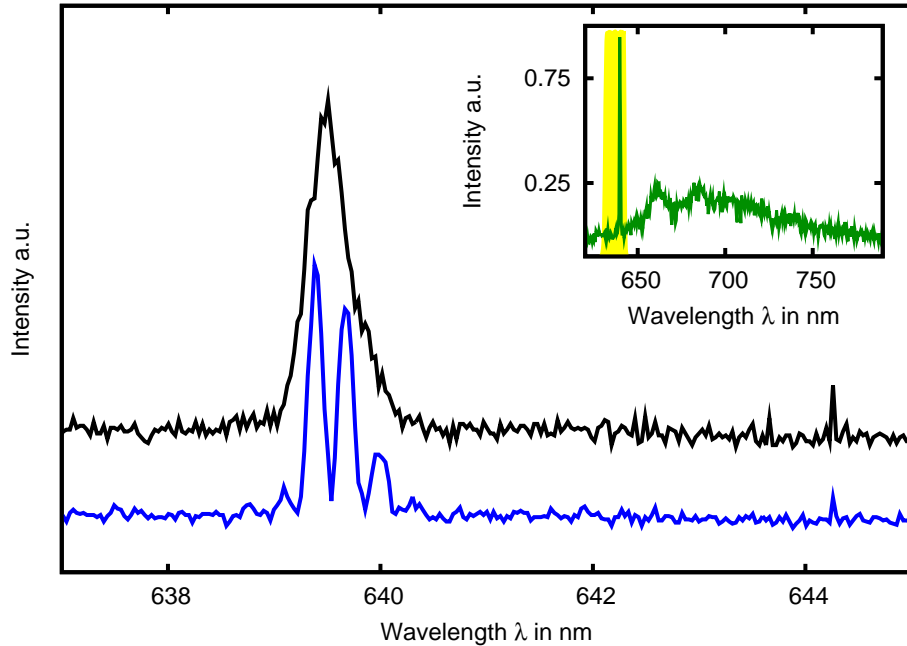


Figure 7.4: Spectra of interferometric-modulated (blue line) and non-modulated (black line) ZPL lines, acquired at 4.8K with integration time of 5 sec. and under 13 μw CW-green excitation.

ond order autocorrelation function was acquired with an integration time depending on the fluorescence intensity. Longer times give better signal to noise ratios, but disadvantages include eventual ionization of NV centers, impurity contamination or objective degassing into the vacuum chamber. Hence, a compromise between practical safety and data accuracy had to be made. During data collection (photon counting), sample out-of-focus drifts arising from mechanical vibrations were compensated via translations of the motorized lens (that means translations of the confocal volume) or piezo-driven objective steps toward the surface. A practical measurement was, in this phase, 5 to 15 minutes long. By reinserting the 7 nm bandpass filter, light collection was performed only with photons generated in the ZPL, that were thus interfering in the Mach-Zehnder. Second order cross-correlation could be obtained from such measurements. As just 3% to 5% of the radiation is emitted within the ZPL, lower countrates imposed a

longer integration time for this step, generally of 30 \div 40 minutes, in order to have reasonable signal to noise ratios and sufficient temporal resolution. Finally, the spectrometer could be used to get a ZPL profile and compare it with the initial one, checking eventual compromising line drifts. Data acquisition was performed by means of a PicoQuant TimeHarp Software, which was recording the photon arrival times for each channel (APD). The so-obtained arrival times were processed by a correlator calculating either the $g^2(\tau)$ and the $g_{LR}^2(\tau)$ functions for a parametrized delay range (spectral diffusion was expected to happen on a timescale going from hundreds of nanoseconds to few milliseconds). A practical example is shown below, where a single NV center was excited with 532 nm light at 25,8 μW and autocorrelation and cross-correlation functions were taken in 10 minutes and 30 minutes respectively. The average photon count rate was, on the full spectral region (including PSB) circa 20K cts/s, whence the ZPL gave 4,6K cts/s:

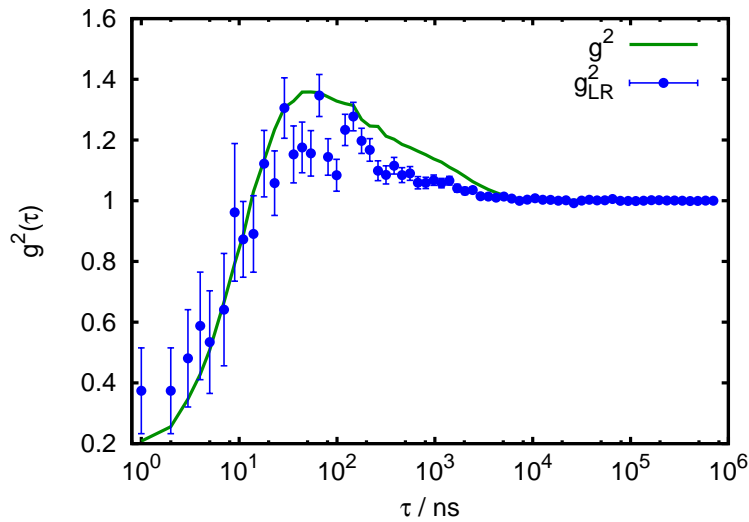


Figure 7.5: The plot shows a non-modulated autocorrelation function (green) for a single NV ZPL emission line, while the blue dots represent the interferometric-modulated cross-correlation function for the same emitter; due to the lower count rate, the associated uncertainty for low time bins is higher.

Where the interferometer effect is clearly observable. By using formulas

5.23, the transition-linked probability function $p(\tau)$ could be estimated:

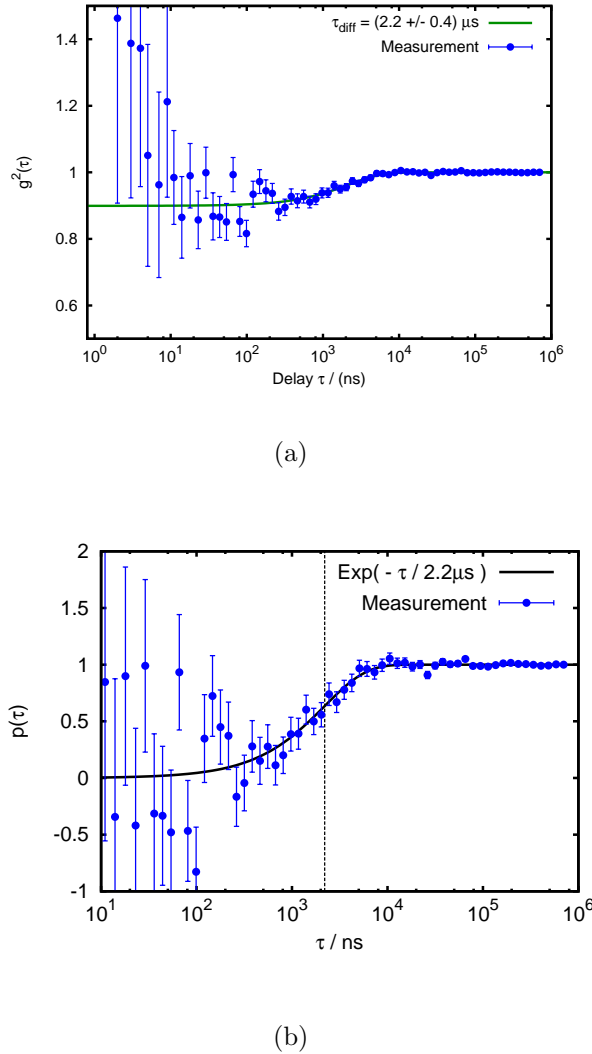


Figure 7.6: Plot of the (τ) calculated as a ratio between the cross-correlation and autocorrelation functions acquired with the procedure described before. In (a) the exponential modulation is clearly visible although reduced by the lower observed contrast, while in (b) a normalization function is used to point out the results.

And an exponential fit gives the average inhomogeneous broadening jump time, confirming the assumption that the forces inducing spectral diffusion are uncorrelated in time. It is possible to see that in the previous emitting system, a spectral jump occurs averagely in $(2, 2 \pm 0, 4)\mu\text{s}$. Different centers were tested repeating the procedure above, giving all coherent infor-

mation; spectral jumps were generally happening on a timescale of $(1 \div 100)$ μs , hence higher than the ZPL countrate itself. An interesting observation comes when calculating from the statistical functions in Fig. 7.6 the interferometer contrast value. A cross-check allows us to see that the evaluated contrasts were lower than the 90% was expected from a spectrometer-assisted visual proof. Such behaviour can be explained by fluorescence background and the static effect of strain in the nanodiamond lattice. As from chapter 3, this induces the removal of degeneracy from the excited states, so that the two main dipole transitions have different frequency (and polarization). On long time scales, the difference in energy averages out and this results in a reduced contrast (by an apparent homogeneous line broadening). The effect could be compensated with a polarizer but only if the excitation/emission radiation is aligned respect to the NV [111] axis; nevertheless, the randomness of nanodiamond spatial configuration makes this solution unpractical.

7.4 Power Dependency Measurements

Correlation between excitation power and spectral diffusion timescale were tested by using a single NV center with a pumping Laser power ramp and keeping the temperature constant. For each value, autocorrelation and cross-correlation functions were acquired and thus the average jump rate within the gaussian envelope calculated. The results are shown in Fig. 7.7:

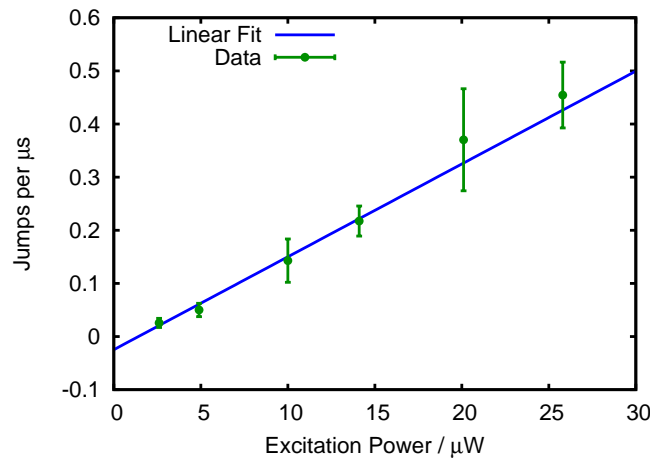


Figure 7.7: Plot of the average number of spectral jumps per microsecond as a function of the 532 nm excitation power

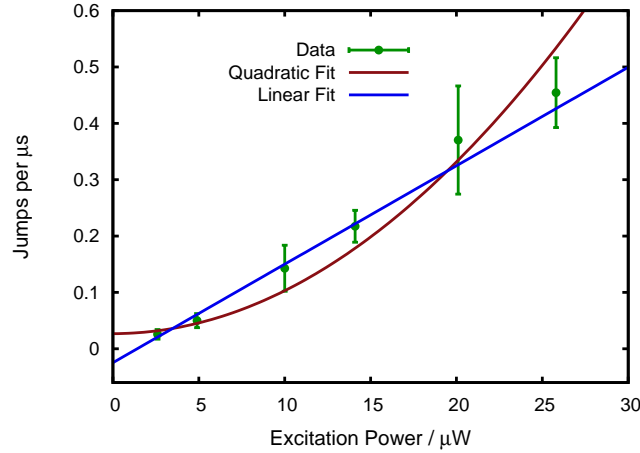


Figure 7.8: Comparison between the linear fit of power-dependency data and quadratic fit. The first one converges better to the experimental results.

and the corresponding obtained values were:

Power (μW)	ZPL countrate(cts/s)	Estimated τ (μs)	Error on τ (μs)
2,6	1100	33,0	9,0
4,9	1600	15,0	4,6
10	2600	6,2	2,0
14,1	3400	4,8	0,8
20,1	4300	2,7	1,1
25,8	4600	2,2	0,4

Table 7.1: Summary of the results obtained from the power dependency measurement.

and show a linear dependence of the average number of jumps per microsecond with the excitation power. By leaving the intercept free, it is possible to notice that the number of spectral jumps per time goes toward zero (within the error limits) suggesting thus that the excitation light might trigger charge fluctuations proximal to the NV center, by i.e. ionizing levels or activating charge traps. Another feature is quite important in estimating the performance for QIP applications; the trend in Fig.7.7 shows that using a very weak excitation beam brings to a low number of spectral jumps per microsecond. However, this decrease is compensated by a lower emission rate in the ZPL; since the relevant parameter for the HOM effect (chapter 1) would be the number of photons emitted between two spectral jumps (so, frequency indistinguishable photons), it is clear than the weaker is the pumping beam, the lower is the jump rate per microsecond and the number of emitted photons in such interval. Thus, in non-saturation regime, reducing the laser power can't be a solution to get an appreciable number of consecutive photons of the same frequency spectra.

7.5 Temperature Dependency

Temperature dependency was partially tested by exciting a single Nitrogen-Vacancy center with 532 nm CW Laser at constant power and calculating the spectral diffusion rates at different specimen temperatures in the range from 5 K to 20 K. Such interval has been chosen considering that above 20K, second order phonon-electron coupling broadens homogeneously [17,38] the ZPL reducing thus the interferometer contrast and requiring a path read-

justment for every measurement. Four single measurements were performed with the procedure described in section 7.2; integration times were 10 minutes for the autocorrelation and 30 minutes for the cross-correlation data. Nevertheless, the few data obtained showed that spectral diffusion rate is not influenced by temperature in the range we used. However, further measurements in this direction are required, although the stability respect to fluctuations in the low temperature range has been generally observed.

7.6 Color Dependency Measurement

In this phase, we used the Supercontinuum white Laser pulsed source (78 MHz) and a set of 10 nm broad bandpass filters to test the spectral diffusion rate dependency from the excitation frequency. With the new excitation line, the beam alignment had to be done once again, with the sequence already explained in sections 1 and 2 of this chapter. Once the setup was optimized, different single measurements were performed by using each time a specific bandpass filter, in order to excite with light having a well defined frequency range. As the absorption efficiency changes according to the Frank-Condon picture, Laser power has been modulated to obtain a constant ZPL fluorescence of $1,4 \pm 0,2$ cts/s. Autocorrelation and cross-correlation functions were acquired with respectively 10 min. and 30 min. of integration time. The results are summarized in the graphic below: By plotting the number of ZPL-emitted photons between two jumps and the number of jumps per microsecond both respect to the pumping frequency (energy), an interesting behaviour can be observed: Namely, the spectral diffusion rate shows an evident threshold level at 2.3 eV; when exciting with radiation above this energy (corresponding to a wavelength of circa 535 nm), the homogeneous line jump rate increases firmly. Hence, this feature suggests that the excitation Laser might induce charge fluctuations via trap activation or ionization. Such a picture is coherent with the information that have been obtained from the previous temperature-dependency and power dependency measurements.

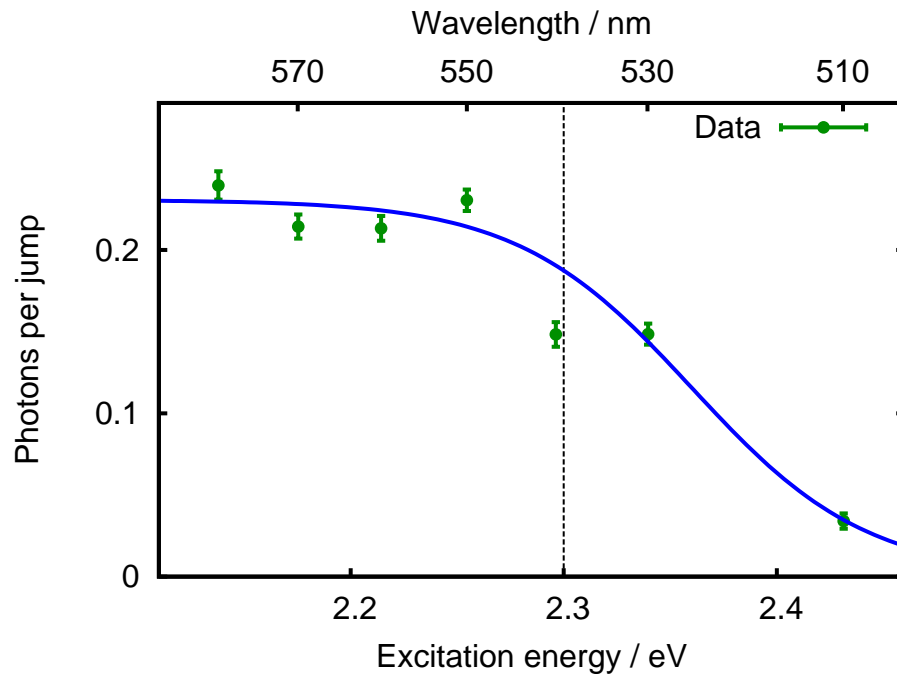


Figure 7.9: Plot of the average photon number emitted on the same line Vs. the excitation energy and wavelength. The increase in the spectral diffusion rate for pumping powers higher than 2,4 eV is clearly visible. The blue line is a guide to the eye.

7.7 Result Summary

The measurements we performed confirmed, at first, that it is possible to measure an average spectral diffusion rate, so an average timescale on which the homogeneous emission line, for the ${}^3E \rightarrow {}^3A_2$ transition in single NV centers, jumps randomly on a frequency space to form the gaussian envelope. The process of inhomogeneous broadening that represents such phenomena has been proven to be triggered by the pumping beam. Furthermore, in the range 5 K to 20 K, it is temperature independent. Finally, exciting the defect with different frequencies shows that the pumping beam photons trigger a 2.3 eV charge trap that induces random electric field fluctuations contributing to the spectral diffusion phenomena as seen in chapter 4. Nevertheless, even if exciting with lower energy, spectral diffusion rate remains on the order of $10^1 - 10^2$ KHz (jumps per second), thus suggesting that the

2.3 eV charge trap is not the only source of environmental electric fluctuations around the emitter.

Chapter 8

Outlook and Conclusions

In this work, quantum information processing was introduced as a new scientific and technological field developed in the late XX century. Some fundamentals of a quantum computer were exposed, as a particular implementation by means of linear optics elements (phase-shifters, polarizers and beamsplitters) and single photons, with the latter carrying information in the form of polarization qubit or dual-rail qubit. Logic gates, and in particular two-qubit gates, are in this picture achievable by using indistinguishable photons that interact in pairs to form maximally entangled states (Hong-Ou-Mandel effect). Nitrogen-Vacancy center in nanodiamond has proven to be a potential candidate as a single photon source for QIP, as its electronic configuration leads to an energy level structure with the ground and excited states lying within the diamond bandgap, hence showing the characteristics of a two level system. Optically-driven transitions between these levels lead to single photon emission, via *transition* radiative decay having the ZPL at 637 nm. Finiteness of the excited state lifetime implies the generated photons to be expressed as non-monochromatic wave-packets; such frequency broadening, called homogeneous, is supported also by fast varying random forces acting on the defect center. However, generally this doesn't represent a serious obstacle toward generation of indistinguishable photons. Instead, a main problem affecting a multitude of solid-state SPS, and the NV center in nanodiamonds too, is inhomogeneous broadening or spectral diffusion arising from emitter coupling with low-frequency fluctuating forces in the external environment. In this project, photon-correlation interferometry

was used to characterize the timescale of such phenomena, as also its dependency from different parameters, in order to gain further knowledge of the underlying processes and elaborate a strategy to control them. Therefore, a Mach-Zehnder interferometer has been implemented to convert the different frequencies of photons after spectral jumps into detectable intensity variations. A Hanbury-Brown-Twiss setup has been used downline to obtain information about the fluorescence light statistics with and without interferometric modulation (that is second order crosscorrelation and autocorrelation functions). From these data, by assuming the low-frequency fluctuating forces acting on the Nitrogen-Vacancy center to be uncorrelated in time, a jump probability (and thus, a jump rate over time) has been calculated. Single measurements have proven to give acceptable, coherent results among them and with the initial assumption. From them, spectral diffusion occurs on a timescale of microseconds, when exciting off-resonantly under saturation and with green 532 CW Laser light. Power dependency measurements have pointed out that the exciting radiation is the main source of spectral diffusion, while temperature, in low ranges, plays no role. Color dependency tests have suggested that the pumping beam might trigger random charge fluctuations in the environment by activating or ionizing traps having definite energy. The charge trap model is supported also by studies on other solid-state SPS, that are quantum dots [53]. In our experiments, a sort of these traps has been located at circa 2.3 eV. From the literature, different diamond defects might be associated with such activation energy, but only one of them is reported to appear in a potentially sufficient concentration to be found within a nanodiamond (which generally has a 40 to 70 nm diameter). This is the negatively charged vacancy interstitial carbon center, which has a ZPL at 2.34 eV [73]. However, more data are required to confirm this suggestion which remains thus highly speculative. Nevertheless, the remaining spectral diffusion is, with high probability, caused by other nitrogen impurities in the lattice, which in type Ib diamond (the one we used) are available at concentration of hundreds of ppm. Single substitutional Nitrogen atoms form donor levels [45][46] ionized at 1.7 eV, which means that even resonant excitation of NV centers (1.945 eV) brings to their activation. Considering our experiments have proven that the jumprate is

circa one to two orders of magnitude higher than the ZPL photon collection rate, we may conclude that further developement is required to make single NV centers in milled nanodiamonds an attractive SPS source for quantum information processing. Strategies that can be outlined involve short-term solutions, which are working with relatively high excitation power (but under saturation) and low excitation wavelength, but also long-term studies on the material developement (as deterministic NV implantation) or on active line stabilization methods, already reported - but not confirmed - for bulk diamond [74]. Furthermore, the effects of nanodiamond surface structure on electronic and optic properties of in-built color centers have to be checked. While it's proven that surface plays a fundamental role in blinking processes in 5 nm to 20 nm large nanodiamonds [75], its role in dynamic electric effects is still not clear. However, understanding the mechanisms that occur at such scale might be helpful not only for the improvement of current SPS sources but also for the implementation of new solid-state single photon emitters.

Bibliography

- [1] A. Einstein, B. Podolsky, N. Rosen, 'Can Quantum-Mechanical Description of Physical Reality Be Considered Complete?', *Physical Reviews*, Vol. 47(10), pp. 777780, 1935.
- [2] E. Schrödinger, M. Born, 'Discussion of probability relations between separated systems', *Mathematical Proceedings of the Cambridge Philosophical Society*, Vol. 31(4), pp. 555563, 1935
- [3] J.S. Bell, 'On the Einstein-Podolsky-Rosen paradox', *Physics*, Vol 1, pp. 195-200, 1964.
- [4]
- [5] D.P. DiVincenzo, 'Two-bit gates are universal for quantum computation', *Physical Review A*, Vol. 51(2), pp. 1015-1022, 1995.
- [6] N.D. Mermin, 'Quantum Computer Science: an Introduction', Cambridge University Press, 2007.
- [7] S.Barnett, Quantum Information, Oxford University Press, 2009.
- [8] M.A. Nielsen, I.L. Chuang, 'Quantum Computation and Quantum Information', Cambridge University Press, 2010
- [9] W.H. Zurek. 'Decoherence, Einselection, and the Quantum Origins of the Classical', *Reviews of Modern Physics*, 75:715775, 2003.
- [10] D. DiVincenzo, *Fortschr. Phys.*, Vol. 48(9-11), pp. 771, 2000
- [11] E. Knill, R. LaFlamme, G.J. Milburn, 'A scheme for efficient quantum computation with linear optics', *Nature*, Vol. 409, pp. 46-51, 2001.

- [12] I.A. Walmsley, M.G. Raymer, 'Toward quantum information processing with photons', *Science*, Vol. 307, pp. 1733, 2005.
- [13] C.K. Hong, Z.Y. Ou, L. Mandel, 'Measurement of subpicosecond time intervals between two photons by interference', *Physical Review Letters*, Vol. 59(18), pp. 2044-2046, 1987.
- [14] Ralph et al., *Physical Review A*, Vol. 75, pp. 022313, 2007.
- [15] J. Zuhang et. al, Exact two-qubit universal quantum circuit, *Physical Review Letters*, Vol. 91, pp. 027903, 2003.
- [16] F. Vatan, C. Williams, 'Optimal quantum circuits for general two-qubit states', *Physical Review A*, Vol. 69, pp. 032315, 2004.
- [17] C. Cohen-Tannoudji, J. Dupont-Roc, G. Grynberg, *Photons and Atoms - Introduction to Quantum Electrodynamics*, John Wiley and Sons, 1989.
- [18] M. O. Scully and M. S. Zubairy, *Quantum optics*, Cambridge University Press, 1997.
- [19] Y. Yamamoto, A. Imamoglu, *Mesoscopic Quantum Optics*, John Wiley and Sons Inc, 1999.
- [20] D.F. Walls, G.J.Milbourn, *Quantum Optics*, Springer Berlin, 1994.
- [21] M. Fox, *Quantum optics: an introduction*, Oxford University Press, 2006.
- [22] M.E. Levinshtein, S.L. Rumyantsev and M.S. Shur, "Properties of Advanced Semiconductors Materials: GaN, AlN, InN, BN and SiGe", John Wiley and Sons, 2000.
- [23] I. Aharonovich et. al, 'Diamond-based single-photon emitters', *Rep. Prog. Phys.* 74, pp. 076501-076529, 2011.
- [24] A. M. Zaitsev, 'Vibronic spectra of impurity-related optical centers in diamond', *Physical Review B* Vol. 61(19), pp. 1290912922, 2000.

- [25] C. Kurtsiefer, S. Mayer, P. Zarda, and H. Weinfurter, 'Stable Solid-State source of single photons', *Physical Review Letters*, Vol. 85(2), pp. 290293, 2000.
- [26] A. Beveratos et. al, 'Room temperature stable single-photon source', *Eur. Phys. J. D* Vol. 18, pp. 191196, 2002
- [27] Classification of Diamond, www.e6cvd.com/cvd, 2012
- [28] F. Jelezko, J. Wrachtrup, 'Single defect centres in diamond: A review', *Phys. Stat. Sol. (a)* 203, Vol. 13, pp. 3207–3225, 2006
- [29] L. M. Pham, N. Bar-Gill, D. Le Sage, C. Belthangady, A. Stacey, M. Markham, D. J. Twitchen, M. D. Lukin and R. L. Walsworth, 'Enhanced metrology using preferential orientation of nitrogen-vacancy centers in diamond', *Phys. Rev. B*, Vol. 86, pp. 121202, 2012
- [30] J. A. Larsson, P. Delaney, 'Electronic structure of the nitrogen-vacancy center in diamond from first-principles theory', *Physical Review B*, Vol. 77, pp. 165201, 2008.
- [31] M. W. Doherty, N. B. Manson, P. Delaney, L. C. L. Hollenberg, 'The negatively charged nitrogen-vacancy centre in diamond: the electronic solution', *New Journal of Physics*, Vol. 13, pp. 025019, 2011.
- [32] A. Lenef, S. C. Rand, 'Electronic structure of the N-V center in diamond: Theory', *Physical Review B*, Vol. 53, pp. 13441, 1996.
- [33] J. R. Maze, A. Gali, E. Togan , Y. Chu, A. Trifonov, E. Kaxiras, M D. Lukin, 'Properties of nitrogen-vacancy centers in diamond: the group theoretic approach', *New Journal of Physics*, Vol. 13, pp 025025, 2011.
- [34] N. B. Manson, J. P. Harrison, M. J. Sellars, 'Nitrogen-vacancy center in diamond: Model of the electronic structure and associated dynamics', *Physical Review B*, Vol. 74(10), pp. 104303, 2006.
- [35] N. R. S. Reddy, N. B. Manson, E. R. Krausz, *Journal of Luminescence*, Vol.38, pp. 46, 1987.

- [36] L. J. Rogers, S. Armstrong, M. J. Sellars, N. B. Manson, 'Infrared emission of the NV centre in diamond: Zeeman and uniaxial stress studies'. *New Journal of Physics*, Vol. 10(10), pp. 103024, 2008.
- [37] V. M. Acosta, E. Bauch, A. Jarmola, L. J. Zipp, M. P. Ledbetter, D. Budker, *Applied Physics Letters*, Vol. 97, pp. 174104, 2010.
- [38] C. Santori, D. Fattal, Y. Yamamoto, Single Photon Application and Devices, Wiley-Wch, 2010
- [39] A. T. Collins, M. F. Thomaz, M. I. B. Jorge, 'Luminescence decay time of the 1.945 eV centre in type Ib diamond', *Journal of Physics C: Solid State Physics*, vol. 16(11), pp. 21772181, 1983.
- [40] J. Wolters et al., 'Enhancement of the zero phonon line emission from a single nitrogen vacancy center in a nanodiamond via coupling to a photonic crystal cavity', *Appl. Phys. Lett.*, Vol. 97, pp. 141108, 2010.
- [41] G. Balasubramanian, P. Neumann, D. Twitchen, M. Markham, R. Kolesov, N. Mizuochi, J. Isoya, J. Achard, J. Beck, J. Tissler, V. Jacques, P. R. Hemmer, F. Jelezko, J. Wrachtrup, 'Ultralong spin coherence time in isotopically engineered diamond', *Nature Materials*, Vol. 8(5), pp. 383, 2009.
- [42] C. Santori, D. Fattal, S. M. Spillane, M. Fiorentino, R. G. Beausoleil, A. D. Greentree, P. Olivero, M. Draganski, J. R. Rabeau, P. Reichart, B. C. Gibson, S. Rubanov, D. N. Jamieson, S. Prawer, 'Coherent population trapping in diamond N-V centers at zero magneticfield', *Optics Express*, Vol. 14(17), pp. 79867993, 2006.
- [43] V. M. Acosta, A. Jarmola, E. Bauch, D. Budker, 'Optical properties of the nitrogen-vacancy singlet levels in diamond', *Physical Review B*, Vol. 82, pp. 201202, 2010.
- [44] K.-M. C. Fu, C. Santori, P. E. Barclay, L. J. Rogers, N. B. Manson, R. G. Beausoleil, *Physical Review Letters*, Vol. 103, pp. 256404, 2009.
- [45] R. G. Farrer, *Solid State Commun.*, Vol.7, pp. 685, 1969.

- [46] Rosa, M. Vanecek, M. Nesladek, *Stals, Diam. Relat. Mater.*, Vol. 8, pp. 721, 1999.
- [47] P. Neumann, R. Kolesov, B. Naydenov, J. Beck, F. Rempp, M. Steiner, V. Jacques, G. Balasubramanian, M. L. Markham, D. J. Twitchen, S. Pezzagna, J. Meijer, J. Twamley, F. Jelezko, J. Wrachtrup, *Nature Physics*, Vol. 6, pp. 249, 2010.
- [48] V. M. Acosta, A. Jarmola, E. Bauch, D. Budker, *Physical Review B*, Vol. 82, pp. 201202, 2010.
- [49] J. Harrison, M.J. Sellars, N.B. Manson, 'Optical spin polarisation of the N-V centre in diamond', *Journal of Luminescence*, Vol. 107, pp. 245248, 2010.
- [50] A. Batalov, 'Low Temperature Studies of the Excited-State Structure of Negatively Charged Nitrogen-Vacancy Color Centers in Diamond', *Physical Review Letters*, Vol. 102, pp. 195506, 2009.
- [51] N.B. Manson, J.P. Harrison, 'Photo-ionization of the nitrogen-vacancy center in diamond', *Diamond and Related Materials*, Vol. 14, pp. 17051710, 2005.
- [52] Ph. Tamarat, T. Gaebel, J.R. Rabeau, M. Khan, A.D. Greentree, H. Wilson, L.C.L. Hollenberg, S. Prawer, P. Hemmer, F. Jelezko, J. Wrachtrup, 'Stark shift control of single optical centers in diamond'
- [53] A. Majumdar, E. Kim, J. Vuckovic, *Physical Review B*, Vol. 84, pp. 195304, 2011.
- [54] M. Stobiska, G. Alber, G. Leuchs, Advances in Quantum Chemistry, Vol. 60 457, Elsevier Inc. 2010.
- [55] Brian J. Smith, M. G. Raymer, 'Photon wave functions, wave-packet quantization of light and coherence theory', *New Journal of Physics*, Vol. 9, pp. 414, 2007.
- [56] T. Legero, T. Wilk, A. Kuhn, G. Rempe, 'Characterization of Single Photons using Two-Photon Interference', *Advances in Atomic, Molecular, and Optical Physics*, Vol. 53, pp. 253-289, 2006.

- [57] K. W. Chan, C. K. Law, J. H. Eberly, 'Localized Single-Photon Wave Functions in Free Space', *Physical Review Letters* Vol. 88(10), pp. 100402, 2002.
- [58] V. Weisskopf, E. Wigner, 'Berechnung der natürlichen linienbreite auf grund der diracschen lichttheorie', *Z. Phys.*, pp. 63:54, 1930
- [59] J. Wrachtrup et al., in Single Molecule Detection in Solution, edited by C. Zander, J. Enderlein, and R. A. Keller, Wiley-VCH, Berlin, 2002.
- [60] Xavier Brokmann,Moungi Bawendi,Laurent Coolen, Jean-Pierre Hermier, 'Photon-correlation Fourier spectroscopy', *Optics Express*, Vol. 14(13), pp. 6333-6341, 2006.
- [61] G. Sallen, A. Tribu, T. Aichele, R. Andr, L. Besombes, C. Bougerol, M. Richard, S. Tatarenko, K. Kheng, J. Poizat, 'Subnanosecond spectral diffusion measurement using photon correlation', *Nature Photonics*, Vol. 4, pp. 696, 2010.
- [62] L. Coolen, X. Brokmann, P. Spinicelli, J. Hermier, *Physical Review Letters*, Vol. 100, pp. 027403, 2008.
- [63] U. W. Pohl et al., in Semiconductor Nanostructures edited by D. Bimberg, Springer, Berlin Heidelberg New York, 2008.
- [64] Y. Shen, T. Sweeney, H. Wang, *Physical Review B*, Vol. 77, pp. 033201, 2008.
- [65] S. M. Mansfield, G. S. Kino, 'Solid immersion microscope', *Applied Physics Letters*, Vol. 57(24), pp. 26152616, 1990.
- [66] W. Barnes, G. Bjrk, J. Grard, P. Jonsson, J. Wasey, P. Worthing, V. Zwiller, 'Solid-state single photon sources: light collection strategies', *The European Physical Journal D*, Vol. 18(2), 197210, 2002.
- [67] S. M. Mansfield, W. R. Studenmund, G. S. Kino, K. Osato, 'High-numerical-aperture lens system for optical storage', *Optics Letters*, Vol. 18(4), pp. 305307, 1993.

- [68] M. Yoshita, K. Koyama, Y. Hayamizu, M. Baba, H. Akiyama, 'Improved high collection efficiency in fluorescence microscopy with a Weierstrass-Sphere Solid immersion lens', *Japanese Journal of Applied Physics*, Vol. 41(27B), pp. L858L860, 2002.
- [69] B. D. Terris, H. J. Mamin, D. Rugar, W. R. Studenmund, G. S. Kino. 'Near-field optical data storage using a solid immersion lens', *Applied Physics Letters*, Vol. 65(4), pp. 388390, 1994.
- [70] A. T. Collins, 'The use of the weierstrass sphere geometry in luminescence spectroscopy', *Journal of Physics D: Applied Physics*, Vol. 10(8), pp. 11431150, 1977.
- [71] T. Schroeder, 'Integrated photonic systems for single photon generation and quantum applications: Assembly of fluorescent diamond nanocrystals by novel nano-manipulation techniques', Ph.D Thesis, HU-Berlin, 2012.
- [72] J. R. Rabeau, 'Single Nitrogen Vacancy Centers in Chemical Vapor Deposited Diamond Nanocrystals', *Nano Letters*, Vol. 7(11), pp. 3433, 2007.
- [73] K. Iakoubovskii, S. Dannefaer, A. Stesmans, 'Evidence for vacancy-interstitial pairs in Ib-type diamond', *Physical Review B*, Vol. 71, pp. 233201 ,2005.
- [74] V. M. Acosta, et al., arXiv:1112.5490 (2012)
- [75] C. Bradac, 'Observation and control of blinking Nitrogen-Vacancy centers in discrete nanodiamonds', *Nature nanotechnology*, Vol. 5, pp. 345-349, 2010.